Investigation of Phase Transition-Based Tethered Systems for Small Body Sample Capture[1]

Marco Quadrelli[2], Paul Backes[3], Keats Wilkie[4], Lou Giersch[5],
Ubaldo Quijano[6], Daniel Scharf[7], Rudranarayan Mukherjee[8]
Jet Propulsion Laboratory, California Institute of Technology, 4800 Oak Grove Drive, Pasadena, CA 91109-8099

This paper summarizes the modeling, simulation, and testing work related to the development of technology to investigate the potential that shape memory actuation has to provide mechanically simple and affordable solutions for delivering assets to a surface and for sample capture and possible return to Earth. We investigate the structural dynamics and controllability aspects of an adaptive beam carrying an end-effector which, by changing equilibrium phases is able to actively decouple the end-effector dynamics from the spacecraft dynamics during the surface contact phase. Asset delivery and sample capture and return are at the heart of several emerging potential missions to small bodies, such as asteroids and comets, and to the surface of large bodies, such as Titan.

Nomenclature

c = specific heat of material
E_M , E_A = elastic moduli of martensite and austenite, respectively.
E_{eff} = effective Young's modulus of the SMA material.
f = contact force
j = electric current
x_A, x_+, x φ = phase fractions
p^{+A}= transition probability from M+ phase to A phase
q = physical displacements
S_V = surface area to volume ratio
S_A, S_M , S_{eff} = effective electrical conductivity
θ = material temperature
θ_0 = temperature of environment
α = convection heat transfer coefficient
α_A, α_M, α_{eff} = coefficient of thermal expansion (CTE) of the SMA material
ε = mechanical strain,
ε_0 = maximum recoverable quasiplastic residual strain
ε^t = phase transition strain within the SMA material
ρ = material density
ξ = instantaneous martensite volume fraction within the material
σ = uni-axial stress
v_x, v_y = components of velocity of spacecraft center of mass with respect to origin of asteroidal body
v_{HS}, v_{VS} = surface components of velocity, at contact point, with respect to origin
Ω = small body angular rate

[2] Corresponding author, Senior Engineer, Mail Stop 198-326, Guidance and Control Analysis Group, , Marco.B.Quadrelli@jpl.nasa.gov, senior AIAA member
[3] Principal Engineer, Sample Acquisition and Handling Group
[4] Senior Engineer, Advanced Deployable Structures Group
[5] Staff Engineer, Deployable Structures Group
[6] Associate Staff Engineer, Deployable Structures Group,
[7] Senior Engineer, Guidance and Control Analysis Group
[8] Senior Engineer, Sample Acquisition and Handling Group

v_{H1}, v_{V1} = components of velocity, at hinge, with respect to origin
v_{H2}, v_{V2} = components of velocity of contact point, at end effector's end, with respect to origin
f_x, f_y = components of control force of spacecraft with respect to origin of asteroidal object
τ = spacecraft attitude control torque
k, c = spring and damper coefficients of a visco-elastic link representing a compliant boom
T, N = tangential and normal components of contact force, at contact point
k_0, c_0 = spring and damper coefficients representing terrain compliance and viscosity.

I. Introduction

In this paper, we investigate the structural dynamics and controllability aspects of an adaptive beam carrying an end-effector which, by changing equilibrium phases, is able to actively decouple the end-effector dynamics from the spacecraft dynamics during the surface contact phase. Asset delivery and sample capture and return are at the heart of several emerging potential missions to small bodies, such as asteroids, and to the surface of large bodies, such as Titan. The objective of this research is to investigate the potential that shape memory actuation has to provide mechanically simple and affordable solutions for delivering assets to a surface and for sample capture and possible return.

Shape memory materials (SMA) possess an interesting property by which the material remembers its original size or shape and reverts to it at a characteristic phase transformation temperature. By training an SMA wire to remember a given straight or curved shape when heated or cooled down to a given temperature, a long wire with low inherent bending stiffness may be ejected or unreeled from a spacecraft and then transformed into a long thin beam via a controlled material phase transition. Once the phase transition has been induced, the wire exhibits a bending stiffness that did not exist before, and the deployed appendage operates now as a stiff robotic arm. Figure 1 shows a conceptual view of how artificial manipulator tensioning would occur via an embedded SM wire, and a proposed sequence for sample capture phase. Conversely, when the phase transition reverses, the original state of string behavior dominated by axial tension is recovered and the appendage can be reeled back inside the spacecraft. The transition is almost perfectly reversible and, in principle, many cycles can be performed reliably, which would enable either deployment of an asset or retrieval of a collected sample. Shape memory phase transition behavior is tailorable, and compositions exist that have been tested at –99 degrees C and below. After plastic deformation at low temperature, the SMA returns to its original configuration upon the supply of heat. The material seems to remember its former shape, which gives the name to the effect. At a higher temperature, another important phenomenon can be observed. Here, the material can be reversibly deformed up to 10% of its original length under a nearly constant load—this behavior is termed superelasticity. Both effects are a consequence of the load-deformation behavior, which is called quasiplastic at low temperature and pseudoelastic at higher temperature. The underlying mechanism of the observed phenomena is a phase transformation between different crystallographic structures, i.e., different variants of the martensite and the austenite phases. A variety of asset deployment of sample capture scenarios would be possible that could potentially minimize the dynamic interactions with the spacecraft during the maneuver. For example, a minimum load of 20 N was shown to be required to be maintained on the end-effector for approximately 2 seconds so that enough soil sample could be collected from an asteroid, which translated in an adverse reaction on the spacecraft and necessitated additional use of the thrusters to correct the attitude at the end of the maneuver. With the new concept, the stiffness of the end-effector arm can be actively modulated so that the back-reaction on the spacecraft can be greatly reduced. Since the rigidity of the link can now be tailored electrically to specific values, innovative scenarios involving different end-effectors can be envisioned that are highly repeatable, simpler in design, with lower mass, power, and cost.

Consequently, we have synthesized the following problem statement: given the spacecraft, manipulator, and terrain models, develop an adaptive control logic and actuator location distribution for the manipulator stiffness that, in conjunction with the attitude and altitude control of the vehicle, decouples the dynamics of the spacecraft from the dynamics of the end-effector while collecting a sample, in a stable manner over a specified amount of time. The adaptive control law is such that the curvature of the manipulator can be modulated over the time the sample has to be collected.

The paper approaches this complex problem sequentially. The first step is the static and dynamic characterization of the component behavior of a shape memory element. The second step is to investigate the system-level characteristics of the problem, in reference to the touch-and-go maneuver that would be necessary for sample collection. In each step, we have followed an analysis phase in conjunction with a testing phase. Hence, a

test-model correlation step is also necessary at each step. In this paper, we describe these initial, albeit necessary steps, before we tackle the more complex problem of closing a control loop around this system.

Section II discusses the coupled Electro-Thermal-Mechanical modeling of shape memory alloy elements. Section III describes the system-level dynamics simulation of the touch-and-go scenario. Se`-+-ction IV describes the hardware tests and model correlation study. Section V provides the conclusion of the paper.

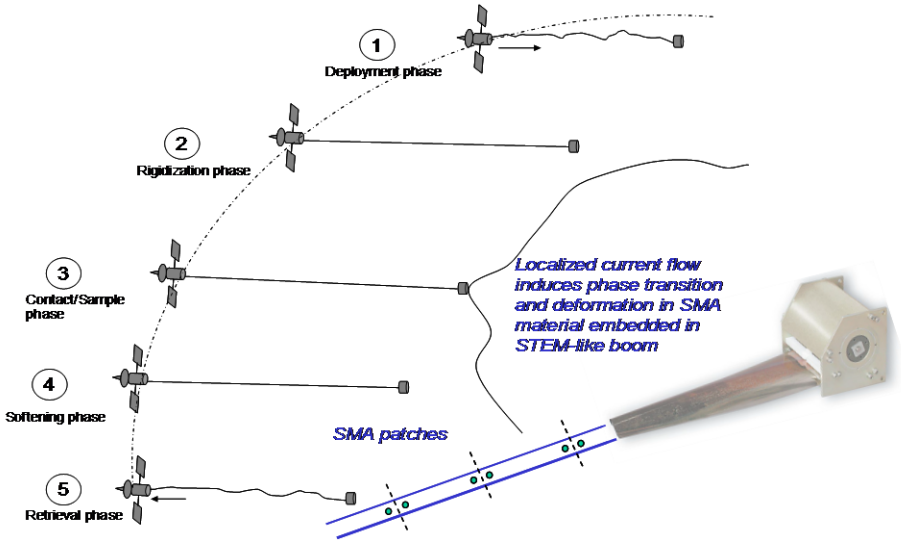

Figure 1. Scenario of Application

II. Coupled Electro-Thermal-Mechanical Modeling of Shape Memory Alloy Elements

In our integrated vehicle dynamics model, we assume that the spacecraft exhibits in-plane dynamics only (3 degrees of freedom), and that it is a rigid spacecraft (no flexibility). The end effector is assumed to contact the surface of the body for a specific duration of time (dwell time), during which the specific mechanics of the sampler device enables the material collection and transmits a horizontal and vertical force to the spacecraft-sampler system. The contact force components are proportional to the horizontal and vertical components of the velocity of the end effector through the static and dynamic friction coefficients of the surface. The manipulator is assumed to act as a massless axial spring that behaves hysteretically, and the properties of the spring are controllable. In the model, we also assume that we can measure the position and attitude of the spacecraft, and that we can measure the contact force. Figure 2 also shows the initial configuration of our multibody dynamics simulation, a system of 10 bodies and 9 rigid links actuated by springs. Summarizing the above assumptions in analytic form, the physics of the system is described by a structural dynamics equation of motion for the physical displacements q in the second order ODE form $\boldsymbol{M}(q)\ddot{q}+\boldsymbol{C}(q,\dot{q})\dot{q}+\boldsymbol{K}(q)q=\boldsymbol{f}(q,\dot{q},t)$, a phase transition balance equation for the phases φ ($\dot{\varphi}=\boldsymbol{g}(\varphi,\sigma,T)$, where σ is the stress on the axial member), and T is the temperature, a thermal balance equation ($\dot{T}=\boldsymbol{h}(T,\varphi,j)$, where j is the current), and the set of initial conditions $q(0)=q_0,\dot{q}(0)=\dot{q}_0,T(0)=T_0,\varphi(0)=\varphi_0$. The actuation inputs are the contact force f, the temperature T, and the current j. In conclusion, for a given applied stress and Joule heat, we can evaluate the phase fractions and the temperature by integrating the system of equations simultaneously, and then calculate the resulting strain. Alternatively, by prescribing strain and Joule heat, we can compute the phase fractions, temperature, and stress.

To achieve the full potential of shape memory actuation, it is necessary to develop models that characterize the hysteretic nonlinearities inherent in the constituent materials. Additionally, the design of SMA actuators necessitates the development of control algorithms based on those models. We have investigated models that quantify the nonlinearities and hysteresis inherent to phase transition, each in formulations suitable for subsequent control design. Candidate models that have been proposed in the past employ either domain theory to quantify phase

transition behavior under isothermal conditions[2,4], or a Muller-Achenbach-Seelecke[10] framework, where a transition state theory of non-equilibrium processes is used to derive rate laws for the evolution of material phase fractions. These models involve first-order, nonlinear ordinary differential equations and require few parameters that are readily identifiable from measurements, hence we have selected to use these differential models in our analysis (see Figure 2 for a simulation of pseudoelastic phase transition behavior).

A. Muller-Achenbach-Seelecke[10] Model

The explicit stress-strain relationship can be derived as follows:

$$\sigma(\varepsilon) = \frac{E_M[\varepsilon - (x_+ - x_-)\varepsilon_0]}{x_+ + x_- + \frac{E_M}{E_A}x_A} \tag{1}$$

The maximum recoverable quasiplastic residual strain ε_0 can be identified from experiment. The evolution of the phase fractions x_A, x_+, x_- is governed by the rate laws:

$$\begin{aligned} \dot{x}_+ &= -x_+ p^{+A} + x_A p^{A+} \\ \dot{x}_- &= -x_- p^{-A} + x_A p^{A-} \end{aligned} \tag{2}$$

where the homogeneity law $x_A + x_- + x_+ = 1$ holds. The quantities in the rates of the phase fractions are transition probabilities, for example, p^{+A} is the transition probability from M+ phase to A phase. The transition probabilities are computed as the product of the probability of achieving the energy required to overcome the energy barrier and the frequency at which jumps are tempted. SMA actuators are typically driven by electric current heating. The temperature change coupled with the mechanical loading triggers the phase transformation between martensite and austenite, and generates the material deformation. Assuming uniform temperature changes through the material, the heat transfer equation becomes:

$$\rho c\dot{T} = -\alpha S_V(T - T_0) - \sigma_R \varepsilon_R (T^4 - T_0^4) + j(t) - (h_{M+} - h_A)\dot{x}_+ - (h_{M-} - h_A)\dot{x}_- \tag{3}$$

where the specific heat c is assumed to be the same for the austenite and martensite phases. The first term is the heat convection to the environment with temperature T_0. The third term is the heat exchanged with the environment by radiation. The fourth term is the Joule heating. The last two terms represent the rate dependent heat generation and loss due to the phase transformation, where the *h*-terms represent the latent heats of transformation of each phase.

The hysteretic constitutive model has been tested numerically under axial loading and thermal input in Matlab® and COMSOL®. The model combines the thermo-electromechanical elements of the SMA behavior in an integrated multi-physics simulation environment (electromagnetic, thermal, mechanical). Simulated pseudo-elastic behavior of SMA tested with the Muller-Achenbach-Seelecke model is shown in Figure 2.

B. Dano-Hyer[2,4] Model

A simple, two-phase phase kinetics model was utilized to represent the material transition behavior of a shape memory alloy filament subject acting under a constant, static tensile load. The phase kinetics model is adapted from one used by Dano and Hyer[2], the thermodynamics of which were developed by Boyd and Lagoudas[4]. The fundamental constitutive equation used for the SMA material element is a modified Hooke's law

$$\sigma = E_{eff}\varepsilon^e = E_{eff}\left(\varepsilon - \varepsilon^t - \alpha_{eff}\left(T - T_0\right)\right) \tag{4}$$

This transformation strain is defined as

$$\varepsilon^t = \varepsilon_0 \xi \tag{5}$$

The martensite volume fraction is itself a function of stress and temperature. For transitions occurring under static loading, it may be solved for directly as a function of temperature using the modified Gibbs free energy relation

$$\xi = \xi(T, \sigma_{stat}) = \left(\sigma_{stat}\varepsilon_0 + \tfrac{1}{2}\Delta a^1 \sigma_{stat}^2 + \Delta\alpha\sigma_{stat}(T - T_0) + \rho\Delta a^4 T - Y\right) / \rho b^1 \tag{6}$$

This relationship is valid only in the transition temperature region between $A_s<T<A_f$, for martensite to austenite transitions, and $M_f<T<M_s$ for austenite to martensite transitions. These transition temperatures are generally functions of stress within the material. A graphical representation of martensite volume fraction as a function of stress and temperature is shown in Figure 3.

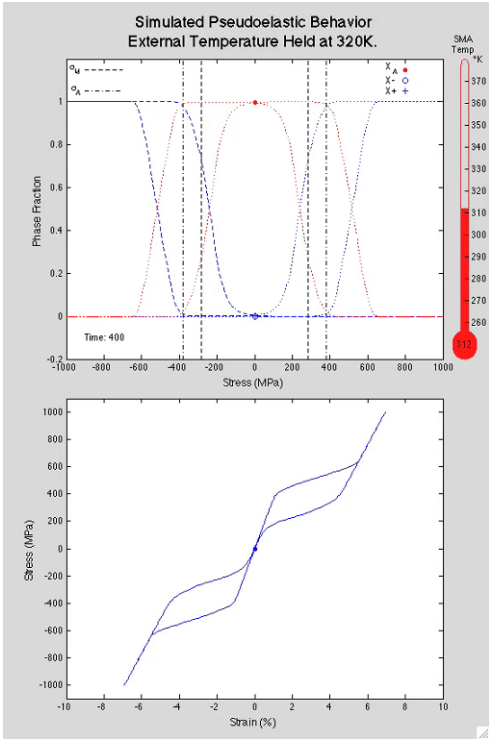

Figure 2. Simulated Pseudo-elastic behavior of SMA tested with the Muller-Achenbach-Seelecke Model.

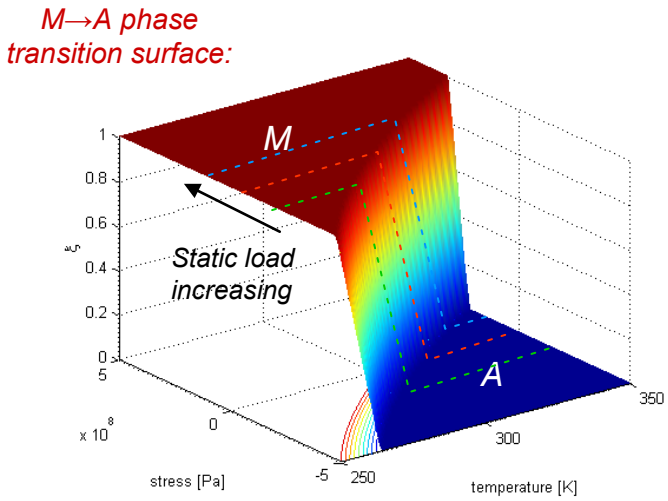

Figure 3. Schematic representation of the martensite to austenite transition surface for ξ, defined by Eq. 3. The martensite volume fraction, ξ, is a function of stress and temperature.

These parameters, as well as effective electrical conductivity, S_{eff}, used in the Joule heating calculations, are determined using simple rules-of-mixtures relations between the instantaneous martensite and austenite volume fractions within the material:

$$\begin{aligned} E_{eff} &= E_A + \xi\left(E_M - E_A\right) \\ \alpha_{eff} &= \alpha_A + \xi\left(\alpha_M - \alpha_A\right) \\ S_{eff} &= S_A + \zeta\left(S_M - S_A\right) \end{aligned} \tag{7}$$

Designing a shape-memory alloy-actuated sample acquisition structure will require an analytical framework capable of modeling the interactions between thermo-elastic mechanics and the material phase transition behavior. For this effort, we have adopted the *COMSOL Multiphysics*[3] computational analysis package for this purpose. COMSOL features discipline-specific physics modules that can be coupled, as needed, at the partial differential equation level. For the simple SMA actuators examined here, the core physics and their primary interactions are modeled using the structural mechanics, heat transfer, and AC/DC modules. To this analytical foundation, a simple two-phase material kinetics model was added. A description of the complete model, developed for exploring the SMA analytical capability of COMSOL, is described below. Correlation of analytical results with a series of simple experiments, designed to identify key material parameters for the SMA materials used throughout this study, are also presented. Values for these and remaining SMA material constants used in Eq. 6 are given in Table I.

III. Hardware Tests

Proof-of-concept hardware was also developed and experiments were performed to demonstrate the fundamental aspects of various SMA deployable structures. These included the bonding of SMA wire to a conceptual STEM boom to demonstrate stiffening of the integrated system, and the Deployable Flexible Segment (DeFS) boom. Experimental testing and demonstration was conducted using optical diagnostics. These included the use of thermal imaging cameras to quantitatively measure the temperatures of the SMA and surrounding structure as well as digital video recorders to qualitatively measure changes in the shape of the proof-of-concept hardware. The DeFS boom was mounted vertically to demonstrate the load conditions over the workspace for small body sampling applications. Quantitative measurements of the shape of the hardware using photogrammetric and/or videogrammetric measurements have also been conducted.

Table I. Shape memory alloy material properties used for COMSOL analysis

symbol	*value/expression*	*description*
E_A	41 [GPa]	Young's modulus, austenite phase
E_M	28 [GPa]	Young's modulus, martensite phase
α_A	11e-6 [1/K]	CTE, austenite
α_M	6.6e-6 [1/K]	CTE, martensite
S_A	1.2e6 [S/m]	Electrical conductivity, austenite
S_M	1.3e6 [S/m]	Electrical conductivity, martensite
A_s	302 [K]	Austenite transition, start temperature
A_f	307 [K]	Austenite transition, finish temperature
M_s	289 [K]	Martensite transition, start temperature
M_f	284 [K]	Martensite transition, finish temperature
ε_0	0.047 [-]	Maximum recoverable plastic strain
ρ	6500 [kg/m^3]	SMA material density
T_0	293.15 [K]	Material properties reference temperature
C_A	41.3e6 [Pa/K]	Critical stress-temperature slope, $M \rightarrow A$
C_M	12.4e6 [Pa/K]	Critical stress-temperature slope, $A \rightarrow M$
k	18 [W/m/K]	SMA nominal thermal conductivity
C_p	600 [J/kg/K]	SMA nominal specific heat
e	0.8 [-]	SMA nominal surface emissivity
h	150 [W/m^2/K]	Surface heat transfer coefficient, SMA→ambient
Δa^1	$1/E_M - 1/E_A$	Martensite-austenite compliance difference
Δa^4 $(M \rightarrow A)$	$-C_A\varepsilon_0/\rho$	Specific entropy, $M \rightarrow A$
Δa^4 $(A \rightarrow M)$	$-C_M\varepsilon_0/\rho$	Specific entropy, $A \rightarrow M$
$\Delta\alpha$	$\alpha_M - \alpha_A$	Martensite-austenite CTE difference
b^1 $(M \rightarrow A)$	$-\Delta a^4 (A_f - A_s)$	Isotropic hardening parameter, $M \rightarrow A$
b^1 $(A \rightarrow M)$	$-\Delta a^4 (M_s - M_f)$	Isotropic hardening parameter, $A \rightarrow M$
Y $(M \rightarrow A)$	$\rho\Delta a^4 A_f$	Latent heat of transformation, $M \rightarrow A$
Y $(A \rightarrow M)$	$\rho\Delta a^4 M_s$	Latent heat of transformation, $A \rightarrow M$

C. 13 mils Diameter SMA Wire Results

Figure 4 shows the 13 mils (0.3302 mm) diameter SMA wire setup. The setup consists of the SMA wire, Keyence laser head, FLIR thermo camera, Agilent DC power supply and dead weights. The SMA wire thickness measured 0.3175 mm (12.5 mils). The overall SMA wire length measured ~52.6 cm (20.7 in). The SMA wire was connected using alligator clips in series with the output of the Agilent DC power supply. The power supply was voltage controlled to insure a constant voltage potential along the length of the SMA wire. Several cases were performed at constant voltages of 5, 4.5, and 4 volts. As the power supply is switched on the SMA wire shrinks and the laser head shown underneath the dead weight records the deflection with respect to time. The total SMA wire shrinkage for a particular case study at 5 volts as illustrated in Figure 4 was 22.5 mm (0.885 in). For this particular case study the SMA wire pulled a combined weight of 1.14 kg (2.51 lbs). Also different case studies were performed using different dead weights. During each case study a FLIR thermo camera was used to capture the temperature gradient of the SMA wire. Figure 8 shows a snap shot of the SMA wire seen by the FLIR thermo camera. The maximum temperature the SMA wire exhibited is around 71 Celsius (160 Fahrenheit). The FLIR camera and the Keyence laser head were synchronous to obtain the temperature versus deflection characteristic plot of the SMA wire.

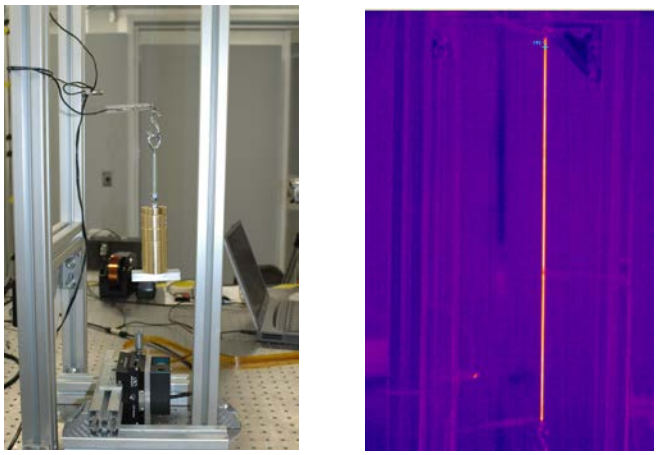

Figure 4. Left: SMA demo setup. Right: Joule heating of SMA wire as seen through thermal imaging camera.

1. SMA actuator configuration and COMSOL analysis description

A simple geometry, shown in Figure 5, was used for investigating general SMA actuation behavior in COMSOL of the test setup depicted in Figure 4. COMSOL 3.5a's pre-built Axial symmetry (2D) Thermal-Electric-Structural Interaction mode was used as the basis for the model. The axial strain equations were modified to include the phase transition strain, as described in Eqs. (4-6). Material modulus and CTE, now functions of the martensite volume fraction, ξ, were determined using Eq. (7). Joule heating of the element, radiative heat transfer, and simplified surface-to-ambient heat convection are represented in the couple model. COMSOL is capable of more sophisticated convective heat transfer modeling, but for simplicity, these features were not exercised here. The COMSOL 3.5a time-dependent segregated solver on default settings was used to solve the resulting coupled quasi-static, transient problem.

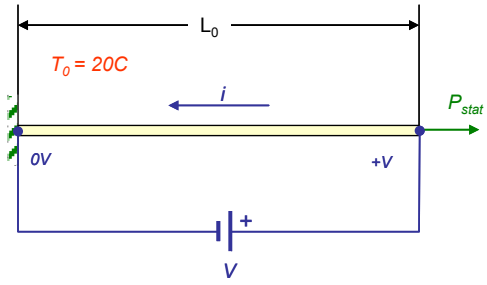

Figure 5. Simple SMA actuator geometry for COMSOL studies. The actuator consists of a thin, cylindrical SMA element of length L_0 under a constant static load, P_{stat}. A fixed voltage, V_0, is applied at one end to produce Joule heating of the SMA element.

2. Model-Test correlation

The COMSOL analysis and simple two-phase material model was able to qualitatively capture the stress and temperature dependent phase transition loop behavior after appropriate tuning of the SMA material parameters using test data. Calculated martensite-to-austenite, and reverse, austenite-to-martensite transition loops for the test geometry are shown in Figure 6 as a function of two applied static loading cases.

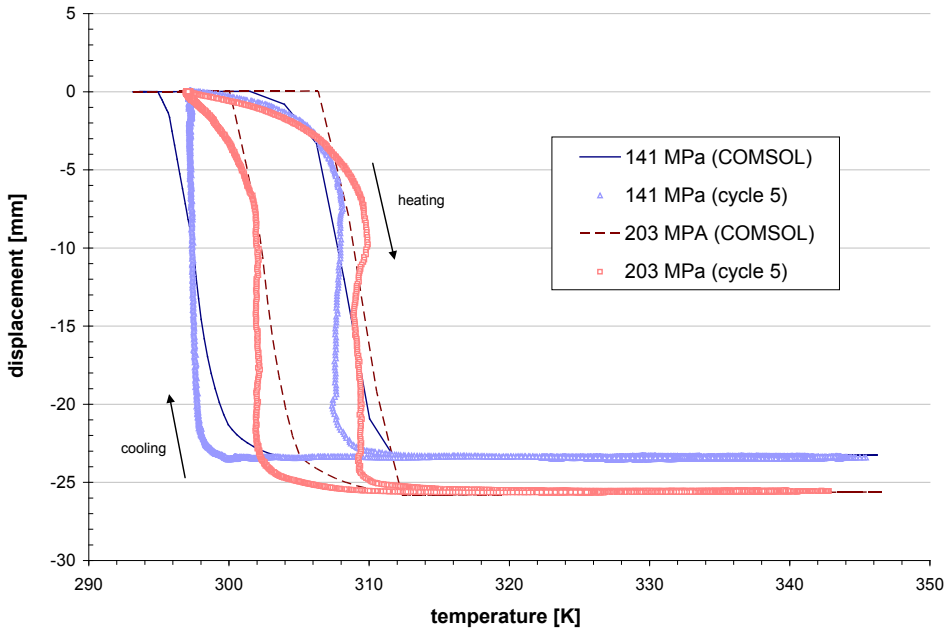

Figure 6. COMSOL predicted displacement-temperature transition loop behavior versus static stress for the test SMA actuator geometry: L_0 = 526 mm; d = 0.3175 mm. Experimental temperatures were obtained using high-speed thermal imaging of the SMA element. Displacement data was obtained using a laser displacement sensor. Sampling interval for the data shown is 0.02 seconds.

Future improvements in the analysis will incorporate a more sophisticated convective heat transfer model, which, although not present in space, will be important for correlation with laboratory test data. Better tuning of the SMA thermal properties is also in order. Finally, to be more generally useful, SMA phase transition behavior will need to be solved for non-static stress loadings, as would be the case in situations where an SMA filament is operating against a spring or elastic flexure, for example, with the Formation Flying Laboratory demonstration test article, described elsewhere in this paper.

D. Pathfinder SMA Experiment Status

A pathfinder experiment was also developed to validate and facilitate the development of the full-scale experiment shown in Figure 7. The pathfinder experiment consisted primarily of a strip of spring steel beam 1" wide, 0.012" thick, and 18" long. A wire of shape memory alloy (SMA) 0.0039" in diameter was attached to the spring steel beam with eyebolts. The SMA wire was routed along the length of the spring steel beam. The beam was then cantilevered off a test fixture (Figure 8). Initial tension in the SMA wire was maintained using turnbuckles attached to the test fixture and each end of the wire, with accommodations made for electrically connecting the SMA wire to a pulsed power supply. The turnbuckles were only used to adjust the tension when the SMA wire was in the Martensite phase; the turnbuckles were not adjusted after the SMA wire was heated to the Austenite phase.

The pulsed power supply consisted of a 0.074 Farad electrolytic capacitor charged to 48 V. When activated by a manual switch, the capacitor discharged through a 1 Ohm current limiting resistor and the SMA wire. The resulting joule heating of the SMA wire was sufficient to transition the SMA from the Martensite phase to the Austenite phase in less than one second. The backside of the beam and test fixture was covered in retro-reflective optical targets to facilitate photogrammetric measurements of the shape of the beam (Figure 8). Photogrammetry is a measurement technique by which the three dimensional shape of an object is reconstructed from multiple photographs of the object taken from different camera locations and orientations. Under proper conditions photogrammetric measurement accuracy can exceed 1 part in 100,000.

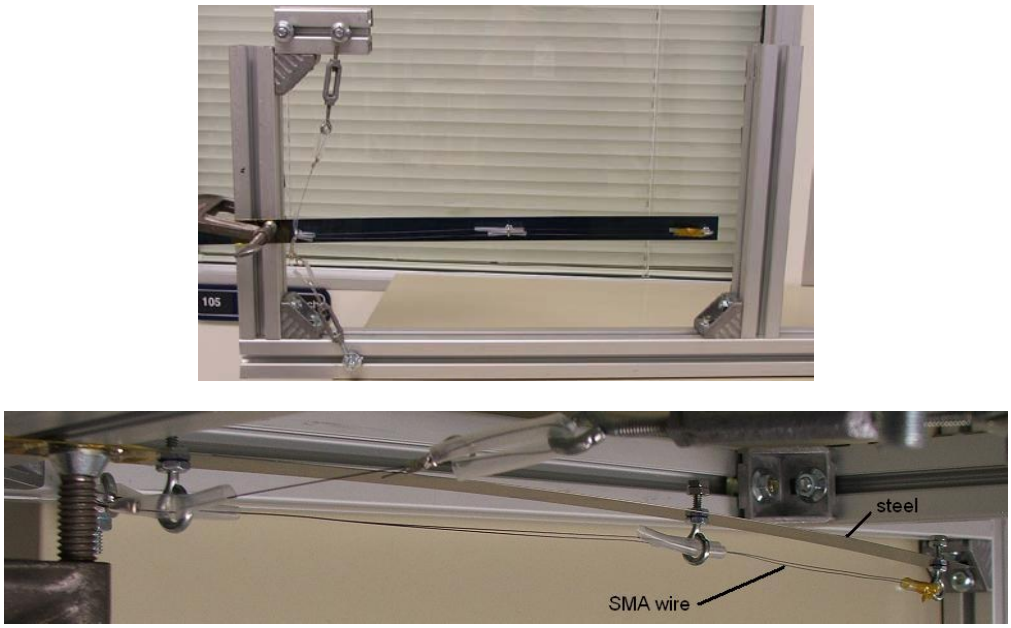

Figure 7. Top: Spring steel beam with SMA wire cantilevered off test fixture. Bottom: Top-down view of the beam and SMA wire.

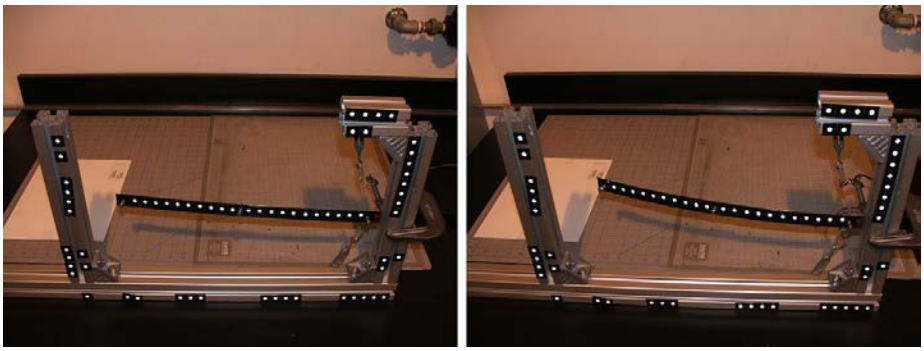

Figure 8. Typical photographs used to measure the shape of the beam with the SMA wire in the Martensite (left) and Austensite (right) phases.

Preliminary photogrammetric measurements of the beam and test fixture were made when the SMA wire was in both the Martensite (cold) and Austensite (hot) phases. Optical targets on the beam yielded data on the three-dimensional shape of the beam both before and after SMA actuation (figure 9). Optical targets on the test fixture yielded reference data and aided in camera calibration, which increased the overall accuracy of the photogrammetric measurements. Although the beam is seen to be slightly bent prior to SMA activation, the bending of the beam is markedly increased after SMA activation.

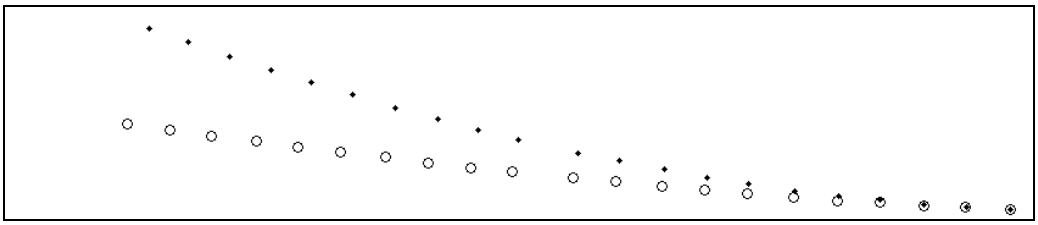

Figure 9. Data from preliminary photogrammetric measurements of the pathfinder demonstrator; 'o' is when the SMA is cold, '•' is when the SMA is hot.

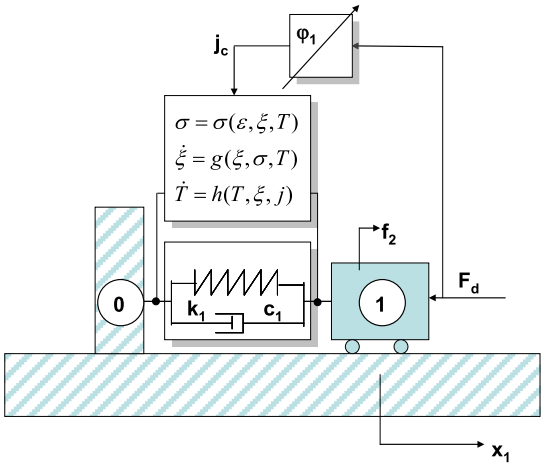

Figure 10. One-dimensional prototype contact problem for external excitation.

IV. Prototype One-Dimensional Dynamics Problem subject to External Excitation

Now that we have a model of the phase-transition behavior of a compliant one-dimensional member, let us investigate the dynamics aspects.

Consider the problem in Figure 10. It represents a prototype one-dimensional problem of a mass connected to a wall by a spring. In particular:

- mass 1 represents a reference mass, with coordinate x_1, acted upon by an exogenous disturbance f_2,
- mass 0 is the ground,
- $\{k_1, c_1\}$ are the stiffness and damping parameters of the spring,
- φ_1 is a control law which, given the actual force magnitude F_d, specifies the electric current j_c which will change the parameters $\{k_1, c_1\}$ of the compliant member.

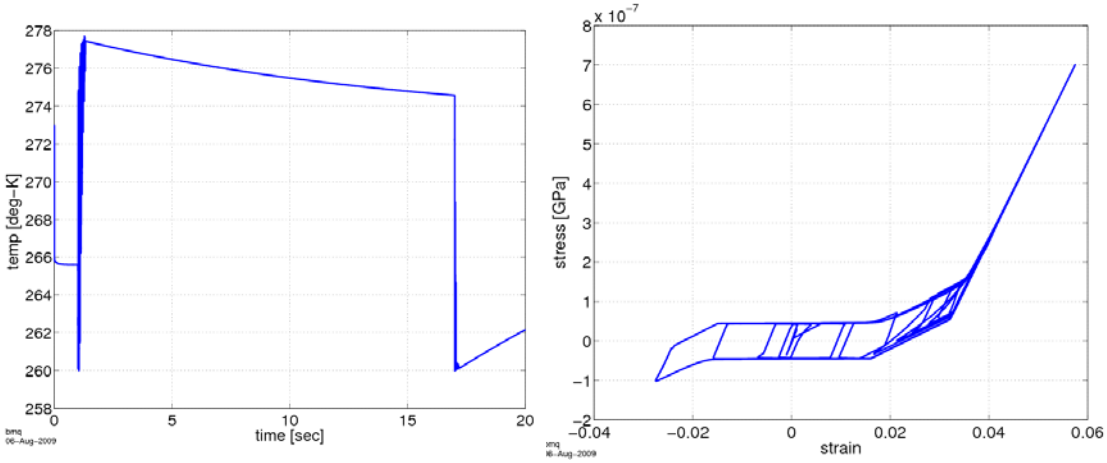

Figure 11. Temperature and stress results of 1D reference case for step input.

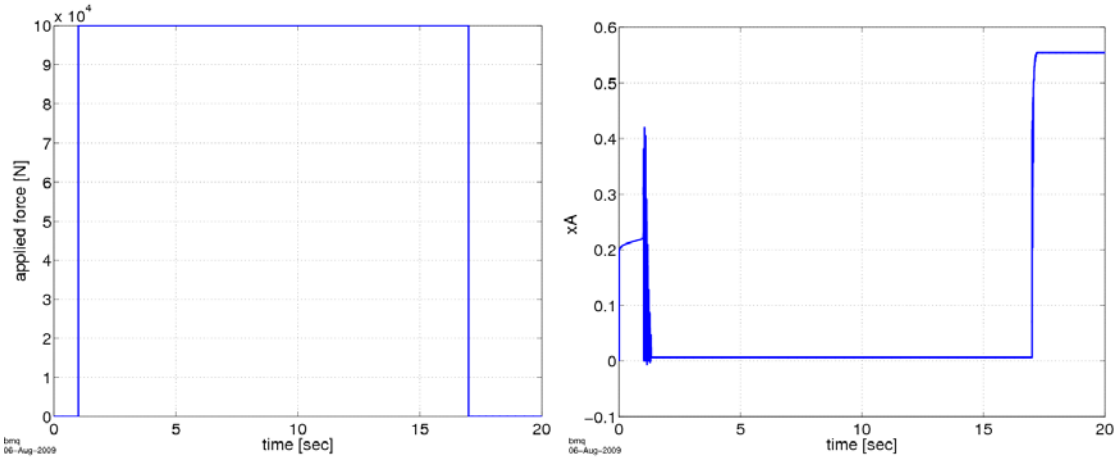

Figure 12. Applied Force and Austenitic phase fraction of 1D reference case for step input.

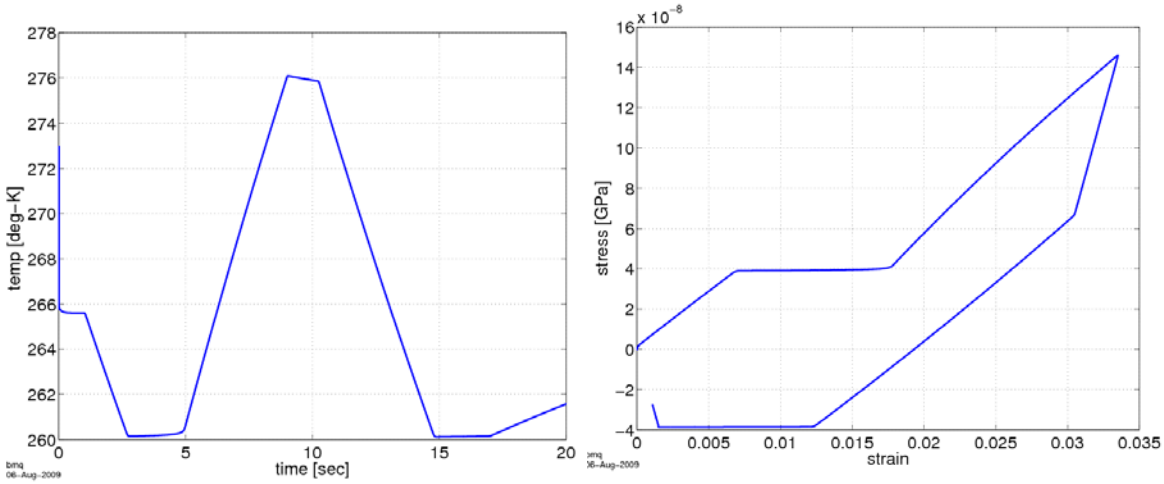

Figure 13. Temperature and stress results of 1D reference case for triangle input.

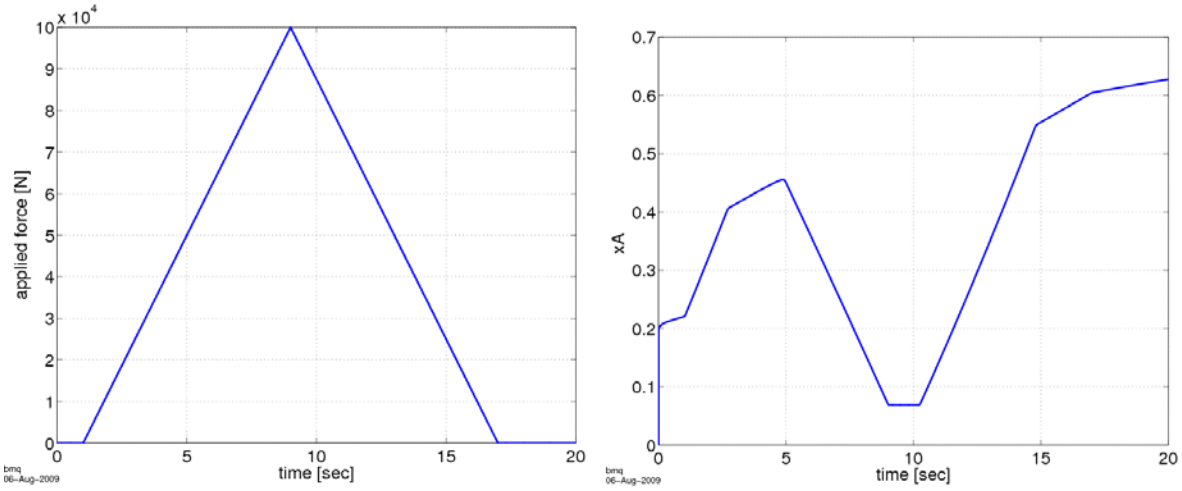

Figure 14. Applied Force and Austenitic phase fraction results of 1D reference case for triangle input.

Figure 11 and 12 show the temperature, stress, applied force, and austenitic phase fraction results for the simulation with a step input. The temperature follows the step command, as well as the austenitic phase fraction, which transitions to martensite for the duration of the step. The stress-strain curve shows a few minor loops during the initial transient. Figures 13 and 14 show the temperature, stress, applied force, and austenitic phase fraction results for the simulation with a triangular input. In this case, the stress-strain curve has time to develop a more hysteretic behavior during loading and unloading. Figure 15 shows the results of the simulation with a sinusoidal input. In this case, the periodic forcing has a clear effect on temperature, phase fractions, and stress-strain.

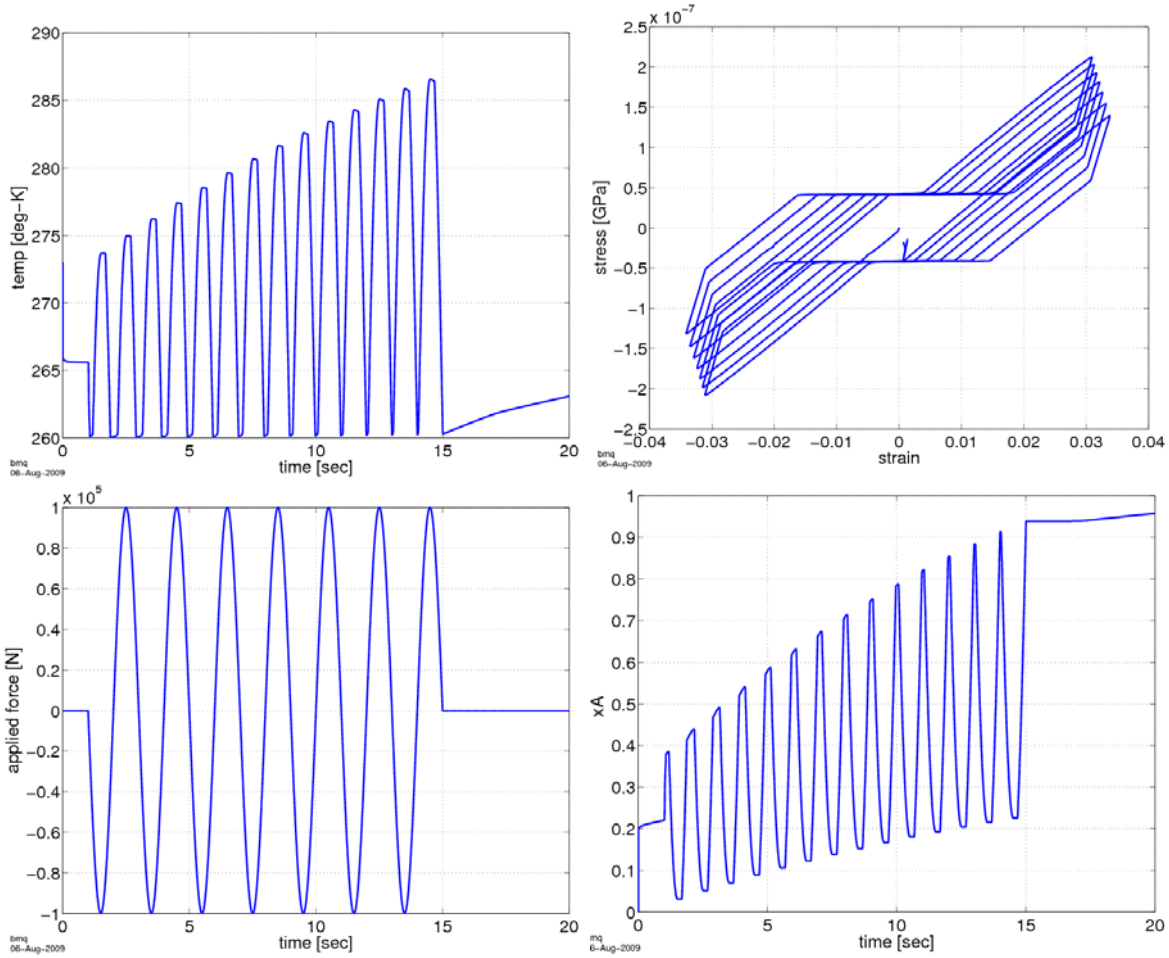

Figure 15. Results of 1D reference case for sinusoidal input.

V. Prototype One-Dimensional Problem for Control during Contact

Now that we have a model of the dynamics of the phase-transition behavior of a compliant one-dimensional member, let us investigate the control aspects by means of a more complex model.

Consider the problem shown in Figure 16. It represents a prototype one-dimensional problem of a vehicle connected via a compliant member to a tip mass which is set to contact a compliant surface. In particular:

- mass 1 represents the spacecraft, with coordinate x_1, acted upon by an exogenous disturbance f_1,
- mass 2 the end effector, with coordinate x_2, acted upon by an exogenous disturbance f_2,
- mass 0 is the ground (or asteroid),
- $\{k_1, c_1\}$ are the stiffness and damping parameters of the compliant appendage,
- $\{k_2, c_2\}$ are the stiffness and damping parameters of the compliant surface which is engaged during contact,
- H is a mapping which gives the mass m_c of collected material (depending on the type of end-effector) once the contact force magnitude F_c is known,

- φ_1 is a control law which, given the error e_F between the desired contact force magnitude F_d and the actual contact force magnitude F_c, specifies the electric current j_c which will change the parameters $\{k_1, c_1\}$ of the compliant member.

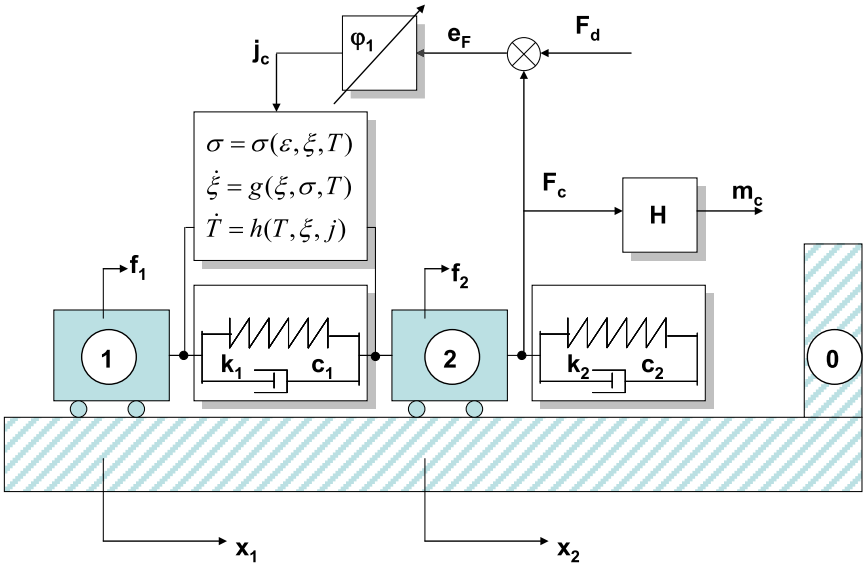

Figure 16. One-dimensional prototype contact problem.

The equations of motion of the open-loop system can be written as follows:

$$
\begin{aligned}
&m_1\ddot{x}_1 + c_1(\dot{x}_1 - \dot{x}_2) + k_1(x_1 - x_2) = f_1 \\
&m_2\ddot{x}_2 + c_1(\dot{x}_2 - \dot{x}_1) + k_1(x_2 - x_1) = f_2 - \gamma(c_2\dot{x}_2 + k_2 x_2) \\
&\gamma = \begin{cases} 0, & \text{before and after contact} \\ 1, & \text{during contact} \end{cases}
\end{aligned}
\tag{8}
$$

The observable vector y of the problem is $y = \begin{pmatrix} x_1 & x_2 & \dot{x}_1 & \dot{x}_2 & F_c \end{pmatrix}^T = CX$, with:

$$
C = \underbrace{\begin{pmatrix} 1 & 0 & 0 & 0 \\ 0 & 1 & 0 & 0 \\ 0 & 0 & 1 & 0 \\ 0 & 0 & 0 & 1 \\ 0 & -\gamma k_2 & 0 & -\gamma c_2 \end{pmatrix}}_{uncertain}
\tag{9}
$$

where $X = \begin{pmatrix} x_1 & x_2 & \dot{x}_1 & \dot{x}_2 \end{pmatrix}^T$ is the system state vector, and the observation matrix C is uncertain, since $\{k_2, c_2\}$ are uncertain. In terms of the state vector X, the open-loop equations are:

$$\dot{X} = \begin{pmatrix} 0 & 0 & 1 & 0 \\ 0 & 0 & 0 & 1 \\ -\frac{k_1}{m_1} & +\frac{k_1}{m_1} & -\frac{c_1}{m_1} & +\frac{c_1}{m_1} \\ +\frac{k_1}{m_2} & -\frac{k_1}{m_2} & +\frac{c_1}{m_2} & -\frac{c_1}{m_2} \end{pmatrix} X + \begin{pmatrix} 0 & 0 \\ 0 & 0 \\ \frac{1}{m_1} & 0 \\ 0 & \frac{1}{m_2} \end{pmatrix} \begin{pmatrix} f_1 \\ f_2 \end{pmatrix} = AX + BU \tag{10}$$

In closed-loop, we have:

$$\begin{aligned} m_1\ddot{x}_1 + c_1(\dot{x}_1 - \dot{x}_2) + k_1(x_1 - x_2) &= f_1 + u_1 \\ m_2\ddot{x}_2 + c_1(\dot{x}_2 - \dot{x}_1) + k_1(x_2 - x_1) &= f_2 - \gamma(c_2\dot{x}_2 + k_2x_2) + u_2 \end{aligned} \tag{11}$$

where u_1 and u_2 are the control forces acting on masses 1 and 2. The characteristics of the compliant member $\{k_1, c_1\}$ are subject to adaptation during contact. Therefore, the proposed control laws u_1 and u_2 are as follows:

$$\begin{aligned} u_1 &= -\varphi_1\left[c_1(\dot{x}_1 - \dot{x}_2) + k_1(x_1 - x_2)\right] \\ u_2 &= -\varphi_1\left[c_1(\dot{x}_2 - \dot{x}_1) + k_1(x_2 - x_1)\right] - F_c \\ F_c &= -\gamma(\underbrace{c_2\dot{x}_2 + k_2x_2}_{uncertain}) \end{aligned} \tag{12}$$

Consequently, in terms of the state vector X, the closed-loop equations become:

$$\dot{X} = \underbrace{\begin{pmatrix} 0 & 0 & 1 & 0 \\ 0 & 0 & 0 & 1 \\ -\frac{\hat{k}_1}{m_1} & +\frac{\hat{k}_1}{m_1} & -\frac{\hat{c}_1}{m_1} & +\frac{\hat{c}_1}{m_1} \\ +\frac{\hat{k}_1}{m_2} & -\frac{\hat{k}_1}{m_2} - \gamma\frac{k_2}{m_2} & +\frac{\hat{c}_1}{m_2} & -\frac{\hat{c}_1}{m_2} - \gamma\frac{c_2}{m_2} \end{pmatrix}}_{uncertain} X + \begin{pmatrix} 0 & 0 \\ 0 & 0 \\ \frac{1}{m_1} & 0 \\ 0 & \frac{1}{m_2} \end{pmatrix} \begin{pmatrix} f_1 \\ f_2 \end{pmatrix} = A_cX + BU \tag{13}$$

Where the modified (phase-transitioned) set $\{k_1, c_1\}$ is:

$$\begin{aligned} \hat{k}_1 &= k_1(1 + \varphi_1) \\ \hat{c}_1 &= c_1(1 + \varphi_1) \end{aligned} \tag{12}$$

which indicates a system state transition matrix that depends on uncertain parameters during the contact phase. Closing a feedback loop under these conditions represents a challenging problem, and will be the subject of future work.

Figure 17 shows the stress-strain curve and heat load results for the 1-D contact simulation with a 10 m long boom. For the same simulation, Figure 18 shows the triangular Joule heat applied and the material temperature. Figure 19 shows the contact load measured by the load cell, and the collected mass as a function of time. Figure 20 shows the austenitic phase fraction and spacecraft angular rate as a function of time. One can see that, for the duration of the contact, the material does not entirely reach a 100% austenitic phase, and that the spacecraft angular rate remains limited to a very small value.

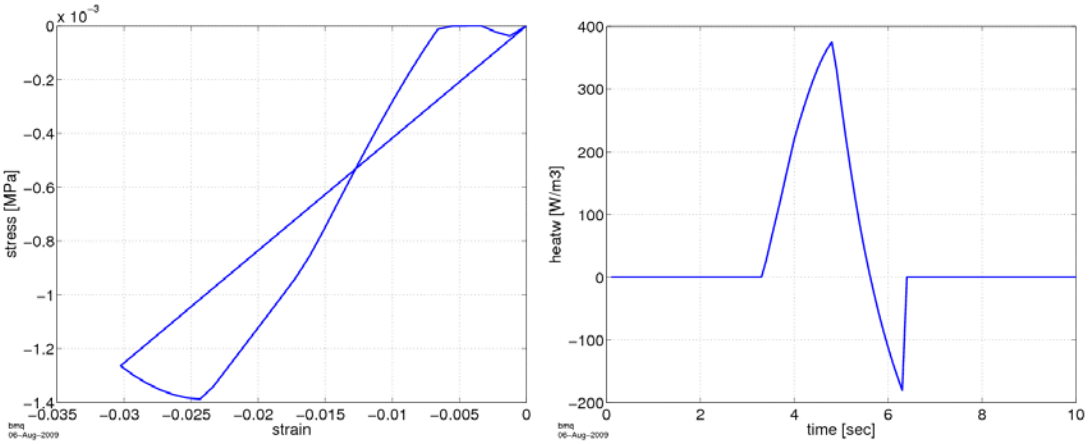

Figure 17. Results of 1D contact problem – 10 m long boom. Stress-strain curve and heat load.

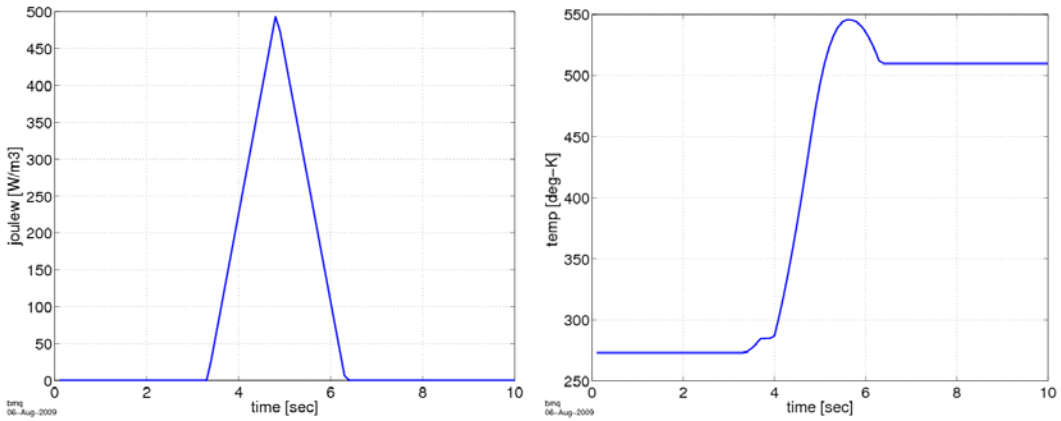

Figure 18. Results of 1D contact problem – 10 m long boom. Joule heat and material temperature.

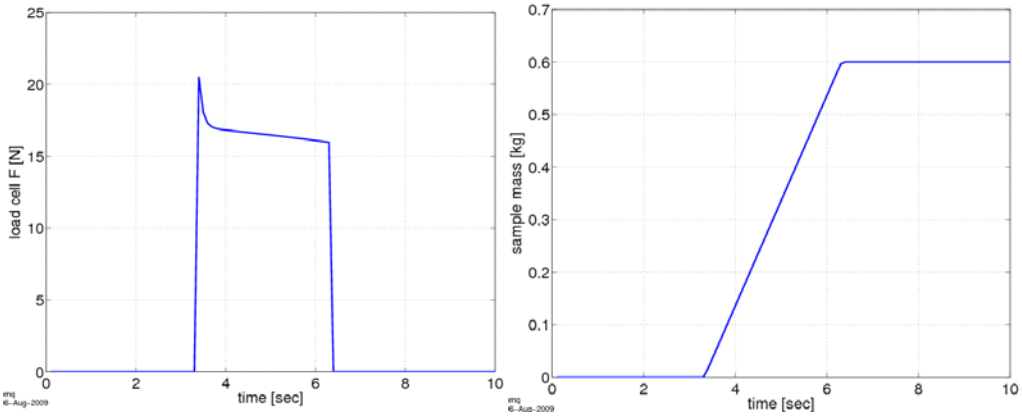

Figure 19. Results of 1D contact problem – 10 m long boom. Load cell measurement and collected mass.

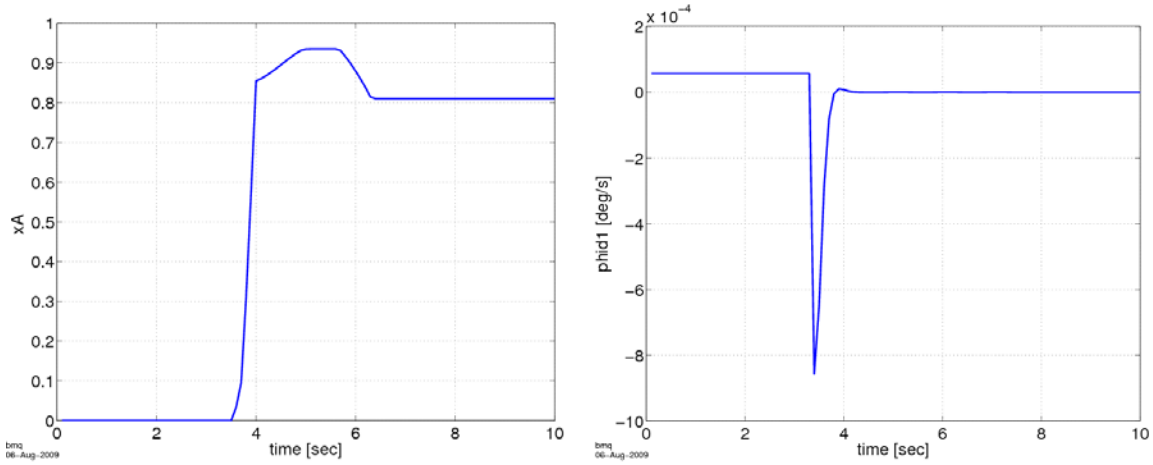

Figure 20. Results of 1D contact problem – 10 m long boom. Austenitic phase fraction and spacecraft angular rate.

VI. Dynamics simulation of touch-and-go scenario

The next step in the analysis is the investigation of the system-level properties of the entire multibody system during contact and feedback loops on. Therefore, a multibody dynamics simulation of the system behavior of the entire vehicle during sample capture has been developed and tested. The objective of the system model is to simulate the zero-gravity planar system-level behavior of the touch-and-go phase of a spacecraft with an attached end-effector at the tip of a long slender boom. The touch-and-go phase involves the end effector approaching a surface, establishing contact with it, and departing from it.

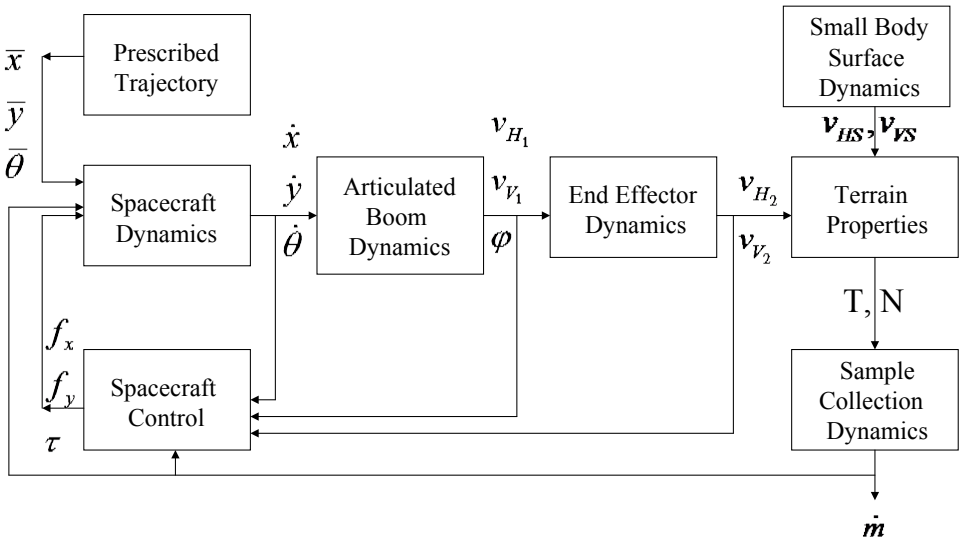

Figure 21. Block Diagram of Integrated Spacecraft/End Effector Dynamics.

Figure 21 shows a block diagram of each element of the Integrated model of Spacecraft and End-Effector dynamics, which includes feedback loops to the spacecraft controller from the hinge states, the end effector states, and the amount of mass collected, assuming all these states are known. If not known, they can possibly be estimated. The reason for including these links is that sensing these states are all possibilities in a scenario where an algorithm

is needed to monitor the duration of the sample event (dwell time), and a change in each one of these states can be used as a trigger to terminate the event. For instance, monitoring the flow of collected mass via a photocell will signal that indeed exogenous matter has entered the spacecraft system, and the event "collect sample" can now be terminated. A change of relative attitude of the end effector or boom angle (or hinge angle) with respect to the spacecraft attitude (as measured with respect to the surface plane) will indicate that the end effector has indeed contacted the ground.

3. Assumptions

In this section, after reviewing the assumptions of the model, we summarize the assumptions used in deriving the equations of motion of the spacecraft with the multibody system connected to the end effector. Figure 22 shows the geometry of the proposed two-dimensional model. Conceptually, a rigid spacecraft may be connected through a revolute (one-axis) joint to an axially compressible boom. The boom is also hinged to the sampler with another one degree of freedom joint. The end effector contacts the surface of the body for a specific duration of time (dwell time), during which the specific mechanics of the sampler device enables the material collection and transmits a horizontal and vertical force to the spacecraft-sampler system. The contact force components are proportional to the horizontal and vertical components of the velocity of the end effector through the static and dynamic friction coefficients of the surface. In Figure 22, x, y represent the components of position of spacecraft center of mass with respect to origin, θ is the spacecraft attitude angle, and φ is boom angle with respect to local vertical. To investigate the dynamic response of the testbed at the system level, a simulation study was carried out under the above assumptions. The simulation study provides an insight on the stability of the system during and after contact.

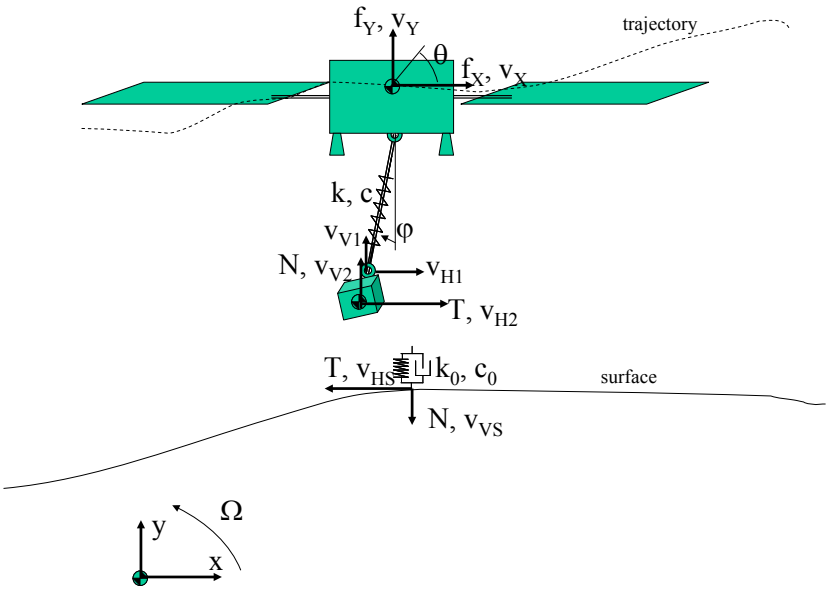

Figure 22. Model of geometry involved in dynamics of sample capture.

We also introduce the contact kinematics variables as follows. The position vector of the surface contact point S, belonging to the terrain, in the inertial frame denoted by the vectrix F_I, is $\mathbf{r}_s$. Similarly, the position vector of the surface contact point H_2, belonging to the end effector, in the inertial frame denoted by the vectrix F_I, is $\mathbf{r}_{H2}$. The contact normal vector is denoted by **n**. Therefore, we define the distance between the two approaching points as $\Phi_n = \left|\mathbf{r}_{H2} - \mathbf{r}_S\right|\mathbf{n}$. The compressive load N can be derived from the contact area A and terrain characteristics (Young's modulus E) as $N = A\sigma$, where σ is the compressive stress and ε the compressive strain. Figure 23 (top) represents the actuated link subject to an axial tension T, where $T = -k(\ell - \ell_0) - c\dot{\ell}$, $k = \dfrac{EA}{\ell}$ is the axial

spring constant, $E = E(\xi, \theta, \ell)$ is the actuated Young's modulus, $\varepsilon = \frac{\ell}{\ell_0} - 1$ is the axial strain, $\dot{\varepsilon} = \frac{\dot{\ell}}{\ell_0}$ is the axial strain rate, and $\ell = \left(\underline{\ell} \square \underline{\ell}\right)^{1/2}, \dot{\ell} = \frac{\underline{\ell} \square \underline{\dot{\ell}}}{\ell}, \underline{\ell} = \underline{r}^{H_1} - \underline{r}^{H_0}$. Also, ξ is one of the phases of the phase transition material, and θ is the temperature, related to the current *i*. For the austenite and martensite phases A is fixed, and E is adapted upon, depending on the length/stress.

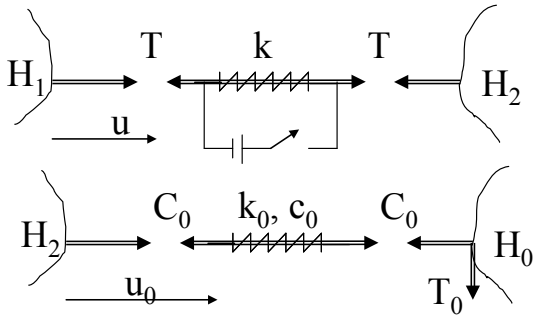

Figure 23. (top) Basic adaptive link dynamics. (bottom) Basic terrain contact dynamics.

Similarly, Figure 23 (bottom) represents the terrain spring subject to an axial tension T_0, where $T_0 = -\mu C_0 sign(\dot{s}), C_0 = -\left[k_0(s - s_0) + c_0 \dot{s}\right], \quad k_0 = \frac{E_0 A_0}{s}$ is the axial spring constant, E_0 is the terrain Young's modulus, and $s = \left(\underline{s} \square \underline{s}\right)^{1/2}, \dot{s} = \frac{\underline{s} \square \underline{\dot{s}}}{s}, \underline{s} = \underline{r}^{H_2} - \underline{r}^{H_0}$. Using the laws of Coulomb (or sliding) friction, given the compressive load N, and (dynamic) terrain friction coefficient μ, we can write that the tangential force is $\tau = -\mu N sign(v_{rel})$. The distinction between sticking and sliding friction can be made at a later stage. This law goes in the block called *Terrain Properties* in Figure 21. Clearly, depending of the relative velocities at the contact point, the terrain characteristics, the duration of the event, and the specific features of the sample collection device, the normal force changes in time and this behavior should also be parameterized.

Tables II, III and IV show a list of representative parameters that we have used for the simulation studies. Table II provides representative system mass and configuration properties (X and Y on floor, Z upwards). Table III gives representative sampler-terrain contact interaction parameters. Table IV gives representative flexible boom parameters. With these parameters, a parametric study has been conducted predicting spacecraft body rates, velocity and acceleration components as a function of: boom stiffness values (EI), contact forces, durations of contact, surface slopes, surface friction coefficients, and spacecraft horizontal and vertical component of approach velocity.

Table V. Representative system mass and configuration properties (X and Y on floor, Z upwards).

Property	Value
Bus Mass [kg]	374.35
Bus moments of inertia about center of mass [kg m2]	34.7347 -0.5298 -0.0300 -0.5298 38.6601 0.8122 -0.0300 0.8122 53.6707
Location of center of mass of Bus above ground [m]	0.291
End-effector (BWS) mass [kg]	30
Bus CM to Boom attachment offset (P) along X [m]	[0.2:0.4]
Bus CM to Boom attachment offset (P) along Z [m]	[-0.2:0.2]

Table VI. Representative sampler-terrain contact interaction parameters.

Property	Value
Range of vertical approach velocity [m/s] along X	[0.1: 0.5]
Range of horizontal approach velocity [m/s] along Y	[-0.1:0.1]
Contact spring stiffness coefficient [N/m]	[1.0:2.0]e4
Contact damper damping coefficient [Ns/m]	[1e1:1e3]
ACS control parameters	Off
Surface slope	[0°:30°]
Surface dynamic friction coefficient	[0.0:1.0]
Duration of contact [s]	[2.0:5.0]
Contact force [N]	[20:30]
SC ascent thrust applied after contact [N]	100
Force sensed by load cell to trigger ascent thruster [N]	5

Table VII. Representative flexible boom parameters.

Property	Value
Mass per unit length [kg/m]	[0.2:0.5]
Length [m]	[3:1000]
Boom material	Aluminum
Young's modulus [N/m2]	70e9
Bending strength EI [N m2]	[100:800]
Structural damping ratio (% of critical)	0.2

4. Numerical results of simulation with fixed configuration and material properties (with phase-transition model disabled)

Initially, we conducted preliminary simulation studies without including the SMA model described elsewhere in this paper. The results of these studies with fixed geometry and material properties were intended to provide insight into the large scale behavior of the system before, during, and after contact, in open-loop. The modeling of the high-fidelity open-loop system was carried out in the Rover Analysis, Modeling and Simulation (ROAMS)[12-13]. ROAMS is a high-fidelity rover simulation environment based on (a) detailed physics based models of the rover mechanical platform including its kinematics and dynamics, (b) its suite of actuators and sensors such as wheel and steering motors and encoders, inertial measurement units, sun sensors, cameras, and (c) models of the environment and the rover's interactions with the environment. The system is modeled as three bodies, which are rigidly connected to each other. The first and third bodies in the system are treated as rigid bodies and model the spacecraft and sampling mechanism. The second body is treated as a flexible body and models the compliant boom that connects the sampling mechanism to the spacecraft. The flexibility of the boom is modeled using the floating frame formulation and retains the nonlinear coupling between the joint displacements and body based deformations. The kinematics and dynamics of the rigid and flexible bodies are modeled using the multibody Spatial Operator Algebra methodology and NASA award winning Dynamics and Real Time Simulation (DARTS) software within the ROAMS framework. The spacecraft retains all 6 degrees of freedom with the rotational degrees of freedom modeled using quaternions, although it primarily is constrained to move in a plane. The second body, i.e., the boom, is modeled using two admissible shape functions, resulting in two degrees of freedom. The system therefore has eight degrees of freedom. The shape functions used are $(x/L)^2$ for the longitudinal degrees of freedom, and $1.5\ (x/L)^2 - 0.5(x/L)^2$ for the transverse degrees of freedom, where L represents the reference length and x is the position of point of interest along the length of the boom. The boom is modeled using clamped-free boundary conditions. The SimScape terrain modeling toolkit[13] within the ROAMS framework is used to model the terrain. A Digital Elevation Map (DEM) represents the terrain (including rocks). ROAMS parameterizes soil mechanics properties using density, internal friction angle and soil cohesion that can be customized to match certain soil types (clay, loose sand, mixed, etc.). The contact model in ROAMS assumes point-plane contact. The terrain under the contact body is assumed to be locally planar and the contact forces are applied to a single point on the body. Two separate and independent non-linear[14] compliance systems are used to compute the contact forces including the normal force and in-plane tangent

forces. This contact model was used to model the interactions of the sampling mechanism with the terrain. The normal force is given by a model such as $F_N = k_N (\delta_N)^n + 3/2\ \alpha_N \dot{\delta}_N (\delta_N)^n$, where F_N is the force in the normal direction, k_N is a spring constant, α_N is a damping constant, n is the non-linear deflection exponent, and δ_N is the deflection and α_N is the rate or time derivative of the deflection. The tangential force is given by a model such as $F_T = k_T \delta_T + d_T \dot{\delta}_T$, where k_T is the spring coefficient, d_T is the damping coefficients and δ_T is the 2D deflection in the tangent plane and δT' is its time derivative[15]. During the initialization of the simulation, the spacecraft is setup above the terrain with specified initial velocity in the horizontal and vertical direction relative to the terrain. Gravity is set to zero. The speeds associated with the flexible body are set to zero. With this initial setup, the spacecraft approaches the terrain and makes contact with it. The resulting contact force on the sampling mechanism is monitored. When this force rises above a specified threshold, the vertical force is applied to the spacecraft to disengage the contact with the terrain. Due to the interaction with the terrain, the system feels contact forces which result in deformation of the flexible boom and attitude and translational motion in the spacecraft. The interaction with the terrain induces rotational motion of the spacecraft. The rotational motion and the contact forces are monitored during the simulation and studied by varying the approach velocity of the spacecraft both in horizontal and vertical direction. Several cases are simulated: 1) flat terrain; 2) 10 degree slope terrain; 3) Axial stiffness=1e4 N/m, lateral stiffness=8e2 N/m (case 1); 4) Axial stiffness=5e3 N/m, lateral stiffness=4e2 N/m.

Figure 24 shows the horizontal and vertical components of the contact force as a function of the approach vertical and lateral velocities for the flat terrain case, and case 1 stiffness. Figure 25 shows the horizontal and vertical components of the spacecraft angular velocity as a function of the approach vertical and lateral velocities for case 1 stiffness and flat terrain. Figure 26 shows the horizontal and vertical components of the contact force as a function of the approach vertical and lateral velocities for the 10 degree slope terrain case, and case 1 stiffness. Figure 27 shows the horizontal and vertical components of the spacecraft angular velocity as a function of the approach vertical and lateral velocities for case 1 stiffness and 10 degree terrain slope. Figure 28 shows the horizontal and vertical components of the contact force as a function of the approach vertical and lateral velocities for the flat terrain case, and case 2 stiffness. Figure 29 shows the horizontal and vertical components of the spacecraft angular velocity as a function of the approach vertical and lateral velocities for case 2 stiffness and flat terrain. The general conclusions of the this parametric simulation study are that the contact loads and SC angular rates for terrain with slope are higher than those with flat terrain, and that lateral forces and lateral angular rates are larger for flat terrain but smaller bending stiffness (more compliant member).

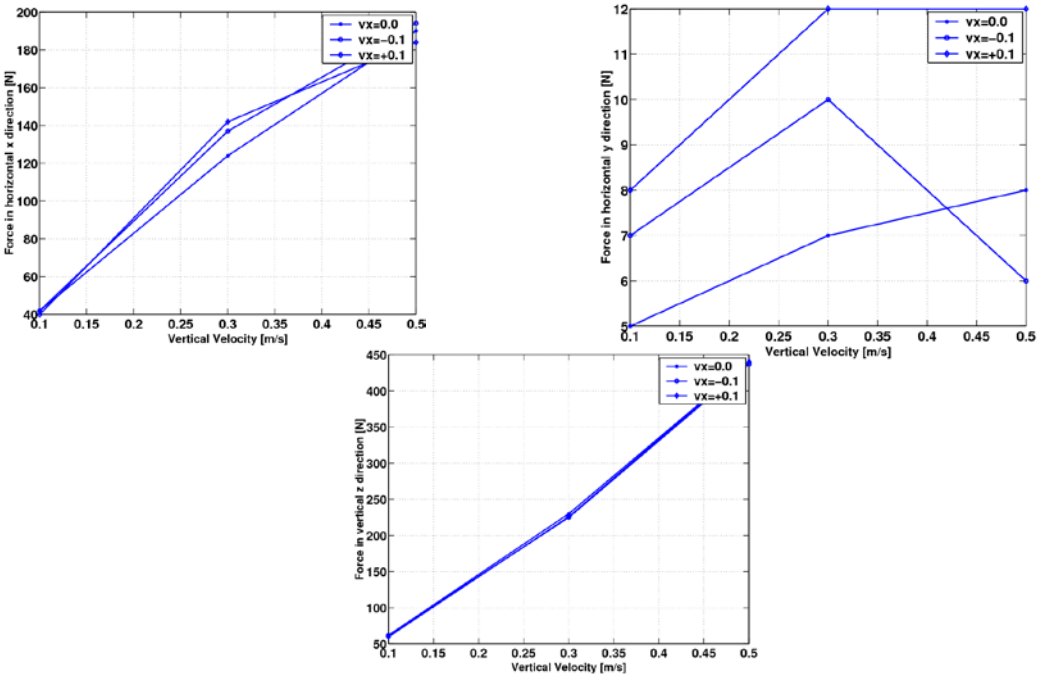

Figure 24. Lateral and vertical contact forces as a function of vertical and lateral approach velocities. Flat terrain case. Stiffness case 1.

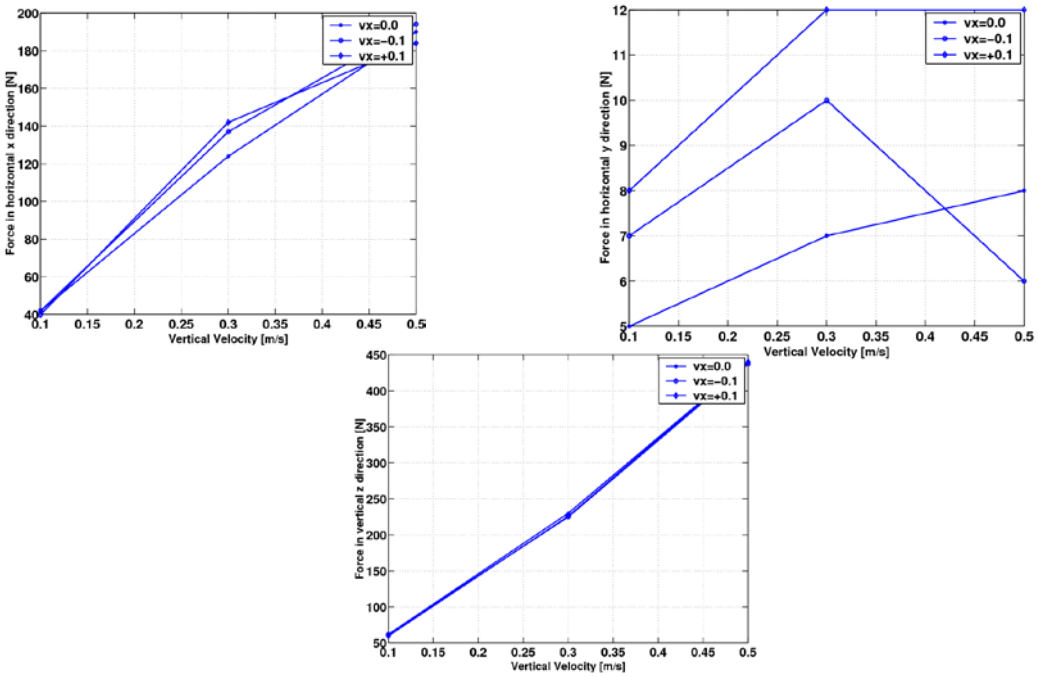

Figure 25. Horizontal and vertical components of the spacecraft angular rate as a function of vertical and lateral approach velocities. Flat terrain case. Stiffness case 1.

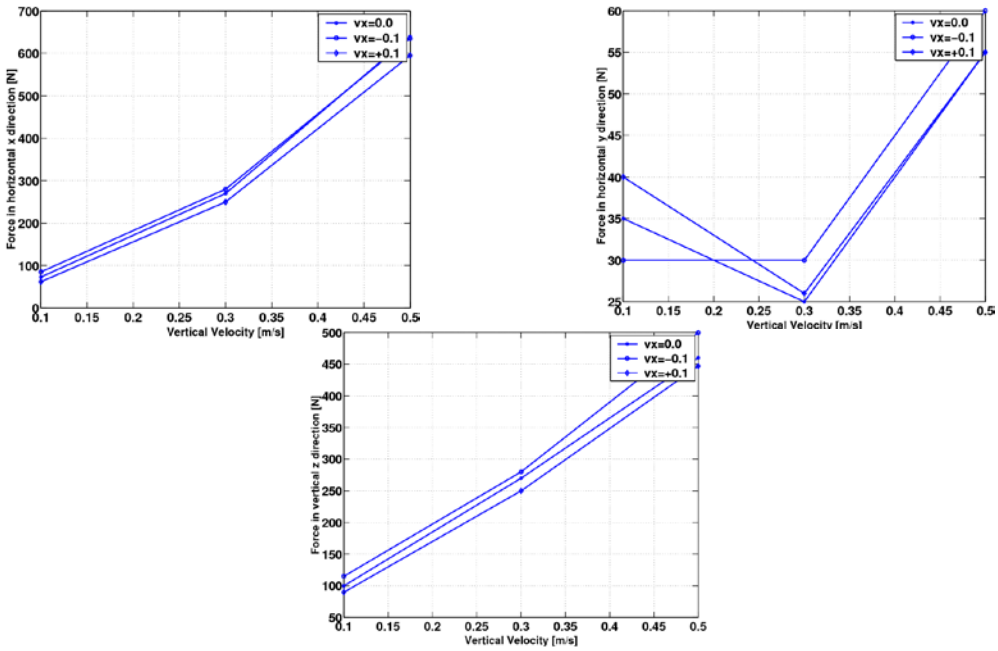

Figure 26. Lateral and vertical contact forces as a function of vertical and lateral approach velocities. 10 degree terrain slope. Stiffness case 1.

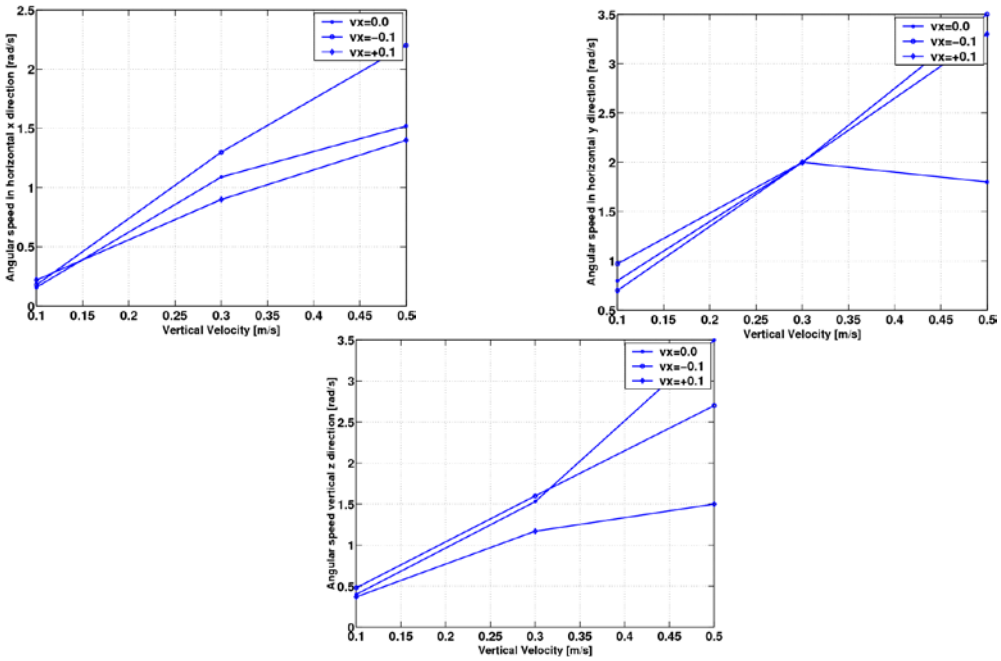

Figure 27. Horizontal and vertical components of the spacecraft angular rate as a function of vertical and lateral approach velocities. 10 degree terrain slope. Stiffness case 1.

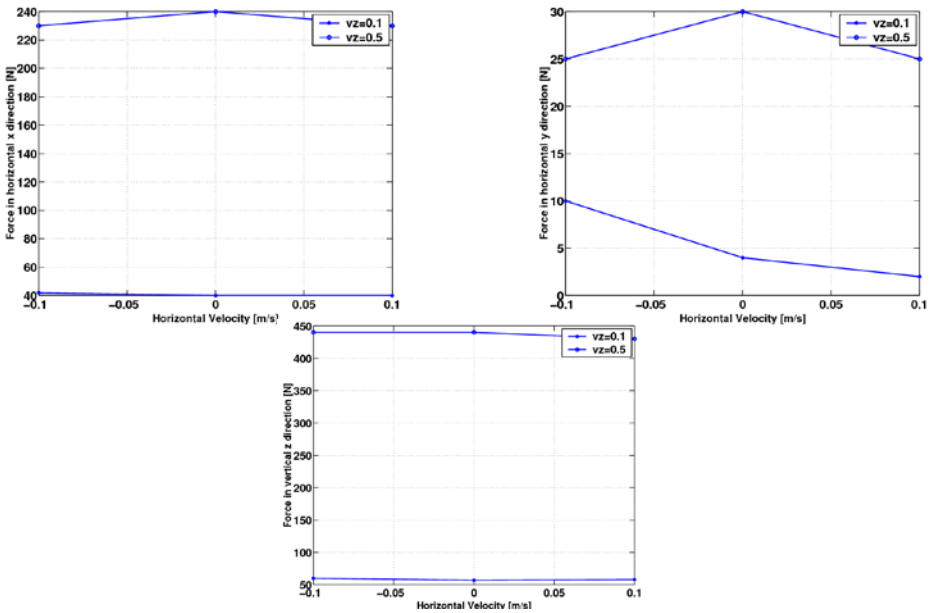

Figure 28. Lateral and vertical contact forces as a function of vertical and lateral approach velocities. Flat terrain case. Stiffness case 2.

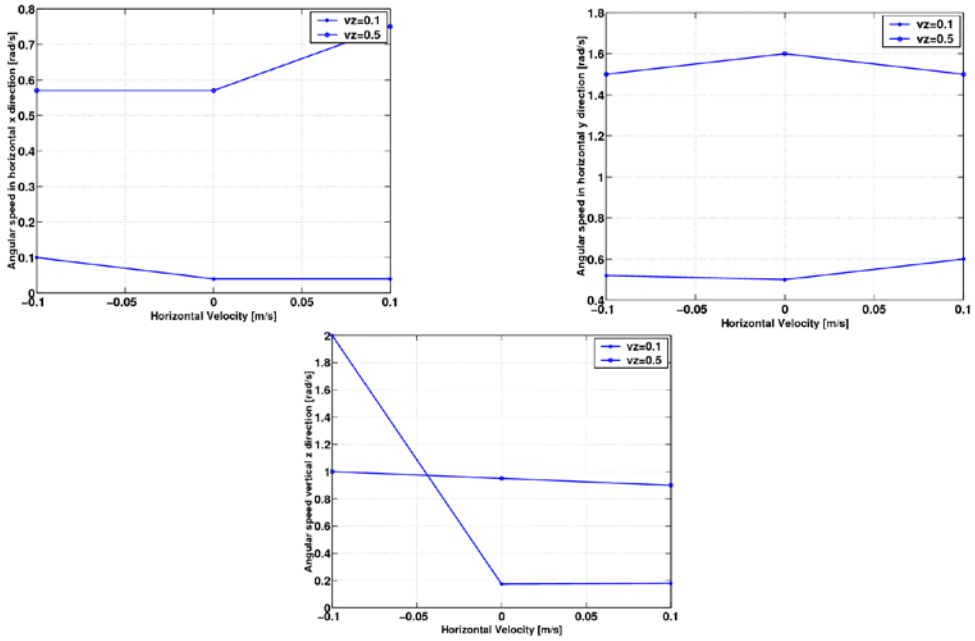

Figure 29. Horizontal and vertical components of the spacecraft angular rate as a function of vertical and lateral approach velocities. Flat terrain case. Stiffness case 2.

5. Numerical results of simulation with fixed configuration and variable material properties (with phase-transition model enabled)

Lastly, we developed another simulation to characterize the behavior of the system with the phase-transition control loop closed. For these preliminary simulation studies, Figure 30 shows the initial geometry of the multibody system.

Figure 31 shows the comparison of spacecraft body rate vs. time for the 4.5 m boom case with and without distributed control. Figure 32 shows the comparison of the spacecraft body rates during contact (indicated by the dotted box) for a 100 m long boom, indicating that there is little effect on the spacecraft attitude rates due to the boom stiffening when control is applied to implement the boom stiffening, since the rates remain well within 0.1 deg/s. Figure 33 shows the comparison of the material stress-strain curve during contact for various lengths. Figure 34 through Figure 38 shows boom temperature, stress vs. strain, mass collected during contact, load measured by the load cell, the spacecraft attitude control torque during the maneuver, and the austeninic phase of the boom material, which transitions from martensite to near full austenite during the touch-and-go maneuver, for the 100 m boom case. Figure 34 shows the temperature and stress-strain curve. Figure 35 shows the collected mass and load cell reading. Figure 36 shows the spacecraft angular rate and austenitic phase fraction. Figure 37 shows the distributed phase-transition control torques along boom and attitude control torque at spacecraft. Figure 38 shows a comparison of the global shape of the 100 m boom configuration without (left) and with (right) distributed phase-transition control.

The results of these analyses is good news, as it demonstrates that contact force modulation through distributed control of the boom elasticity causes weak dynamic coupling with the spacecraft, hence modulation of the sample collection dynamics by means of phase-transition control is feasible.

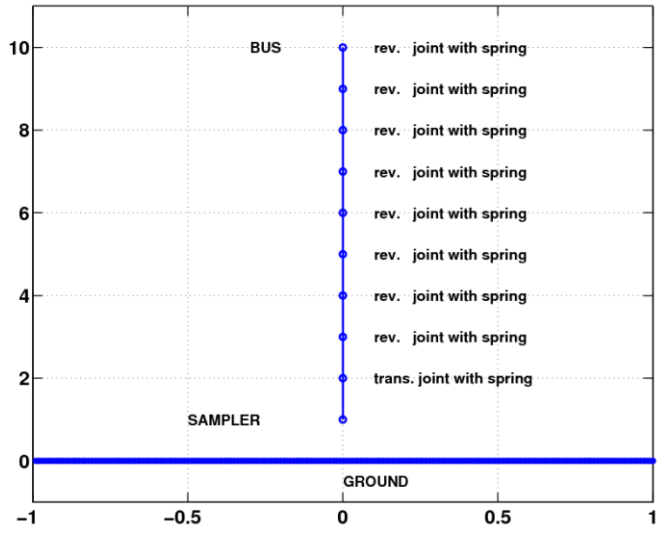

Figure 30. Snapshot of multibody dynamics simulation.

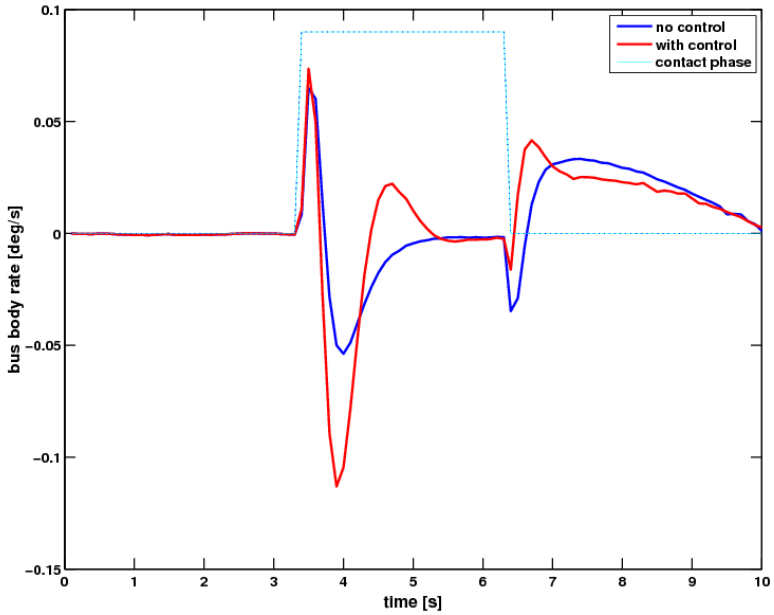

Figure 31. Comparison of spacecraft body rate vs. time for the 4.5 m boom case with and without distributed control.

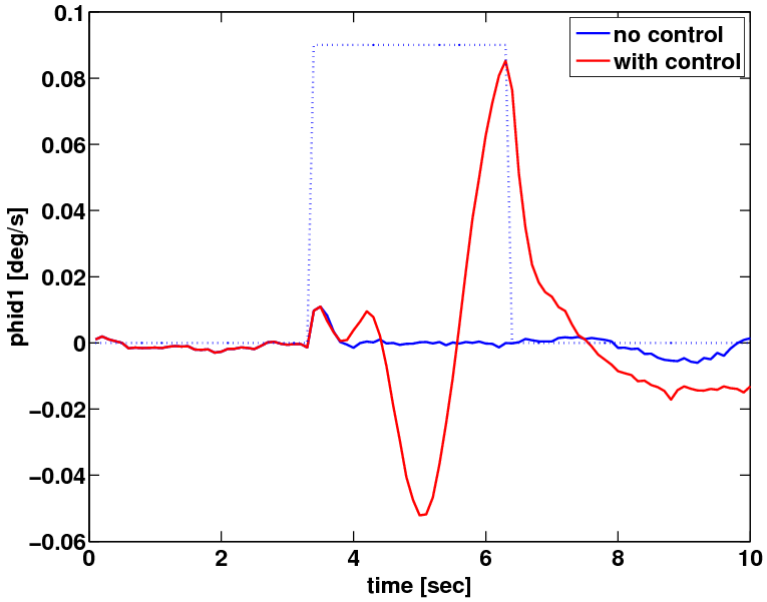

Figure 32. Comparison of spacecraft body rate vs. time for the 100 m boom case with and without distributed control.

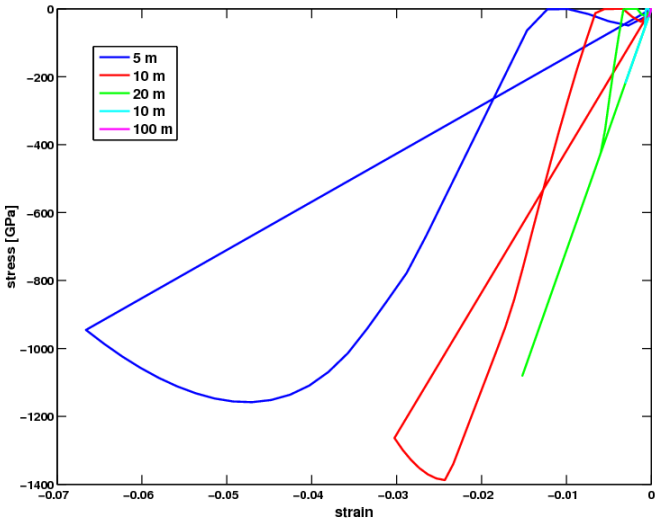

Figure 33. Comparison of material stress-strain curve during contact for various lengths.

VII. Preliminary Experimental System-Level Tests

A plan for the test of the multibody dynamics of the system behavior of the entire vehicle during sample capture has been developed. Similarly to the multibody analysis simulation, the objective of this system model test is to simulate the zero-gravity planar system-level behavior of the touch-and-go phase of a spacecraft with an attached end-effector at the tip of a long slender boom. The touch-and-go phase involves the end effector approaching a surface, establishing contact with it, and departing from it. A sketch of the elements of the testbed that is being used to test the system behavior is shown in Figure 39.

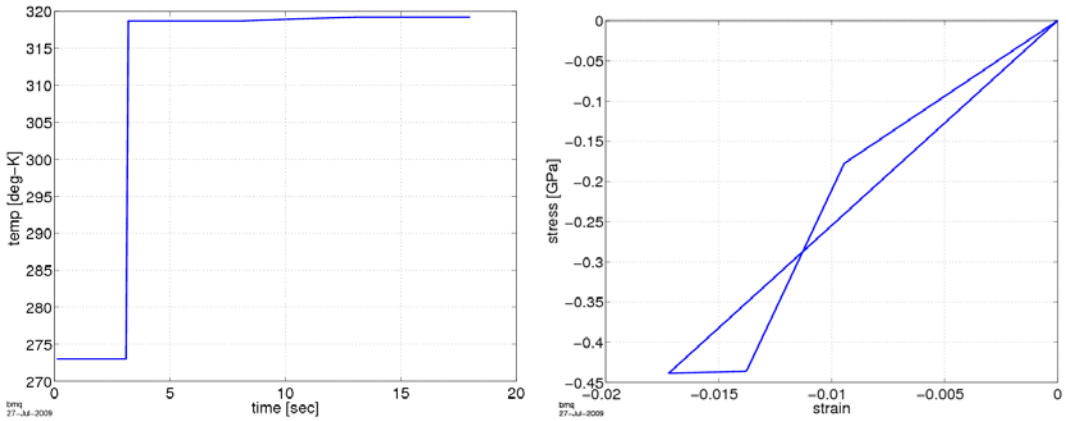

Figure 34. Results of system-level simulation run for 100 m boom length. Temperature and stress-strain curve.

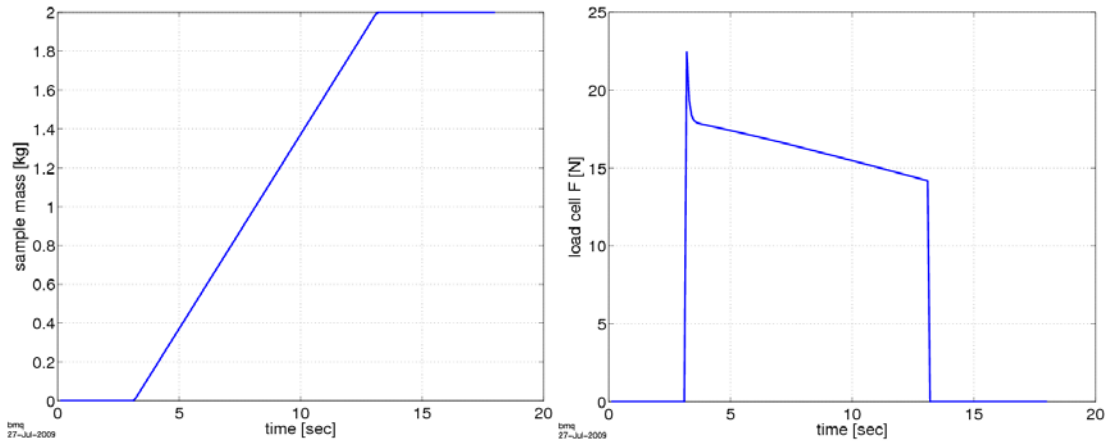

Figure 35. Results of system-level simulation run for 100 m boom length. Collected mass and load cell reading.

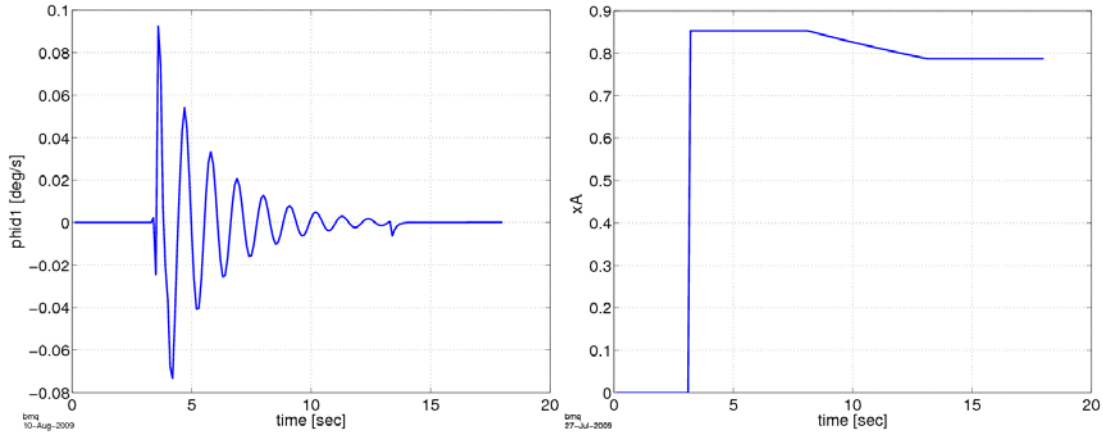

Figure 36. Results of system-level simulation run for 100 m boom length. Spacecraft angular rate and austenitic phase fraction.

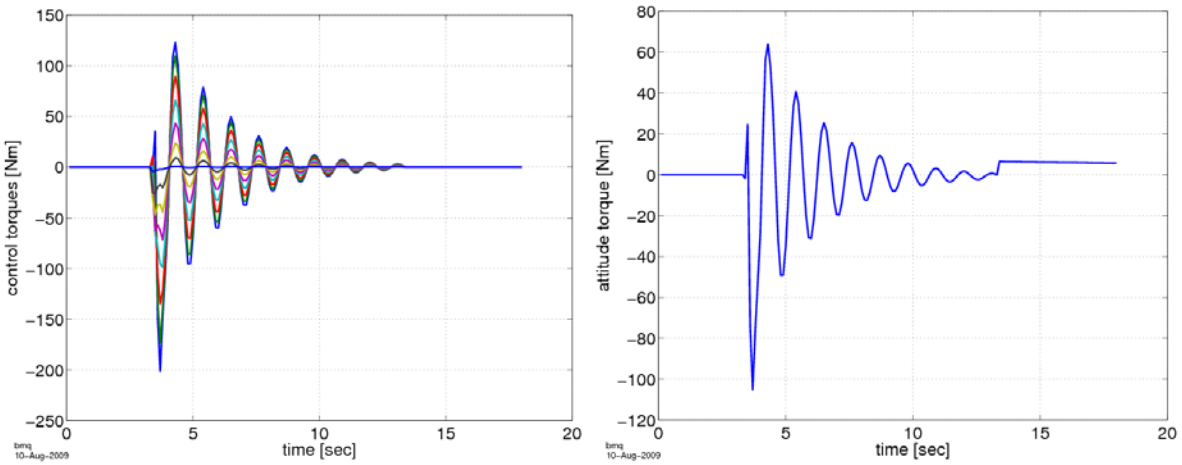

Figure 37. Results of system-level simulation run for 100 m boom length. Distributed phase-transition control torques along boom and attitude control torque at spacecraft.

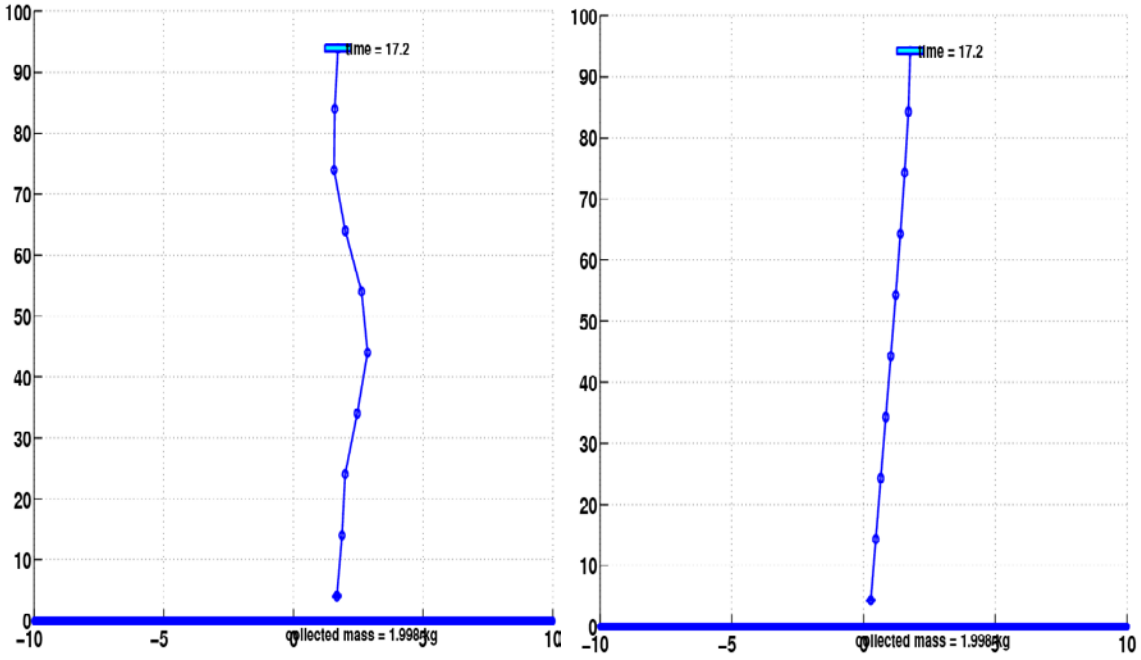

Figure 38. Comparison of global shape of 100 m boom length without (left) and with (right) distributed phase-transition control.

The tests are being carried out in the Formation Control Testbed (FCT) at JPL. The Formation Control Testbed is a multi-robot, flight-like, system-level testbed for ground validation of formation guidance, estimation, and control architectures and algorithms, including autonomous rendezvous and formation infrastructure technologies such as communication protocols and formation sensors[16] . The FCT currently consists of two robots with flight-like hardware and dynamics, a precision flat floor that the robots operate on, ceiling-mounted artificial stars for attitude sensing and navigation, and a ground control" room for commanding the robots and receiving telemetry. While originally conceived for formation-flying ground-demonstrations, the flight-like characteristics of the FCT robots are appropriate for demonstrating a SMA-controlled, small-body sample-gathering impact. A primary robot, part of

the flat floor, and an auxiliary robot are shown in Figure 39. Each of the two primary robots has a lower translational stage (TS) and an upper attitude stage (AS). The TS provides both translational and rotational degrees of freedom to the AS by means of (i) linear air bearings that float an entire robot on a cushion of air a few thousandths of an inch thick, (ii) a spherical air bearing in which a spherical surface on the bottom of the AS floats on a cushion of air generated in a pressurized cup at the top of the TS, and (iii) a telescoping vertical stage provides motion of the AS along the gravity direction in response to thruster commands. Boom deployment will not be considered as the flexible manipulator (boom) is already deployed. Sample retrieval and handling is also not a concern at this stage. The test will provide insight into the feasibility of having a slender flexible manipulator for touch-and-go sampling. We will collect time series data of system level response at low bandwidth (0.8 Hz) using videogrammetry (for boom deflections), and at high bandwidth (> 10 Hz, during the contact phase when we will measure the contact force) using accelerometers and the load cell. This data will be used to correlate the results with those obtained with the analytical multibody model of the system. For the purpose of demonstrating a sample-gathering impact, only the planar characteristics of a primary FCT robot are relevant. The AS is not floated, resulting in a primary robot that behaves as a three degree-of-freedom spacecraft. An auxiliary robot, consisting of a single linear air bearing emulates the sample-gathering mechanism, with an SMA-boom connecting the two. The ratio of mass of the primary robot to the auxiliary robot is approximately 30:1. Prior to subsequent quantitative evaluation, we observed that the entire system, when floated with no friction, exhibits a ~0.5 Hz first mode consisting of attitude oscillations of the primary and auxiliary robots coupled with vibrations in the boom.

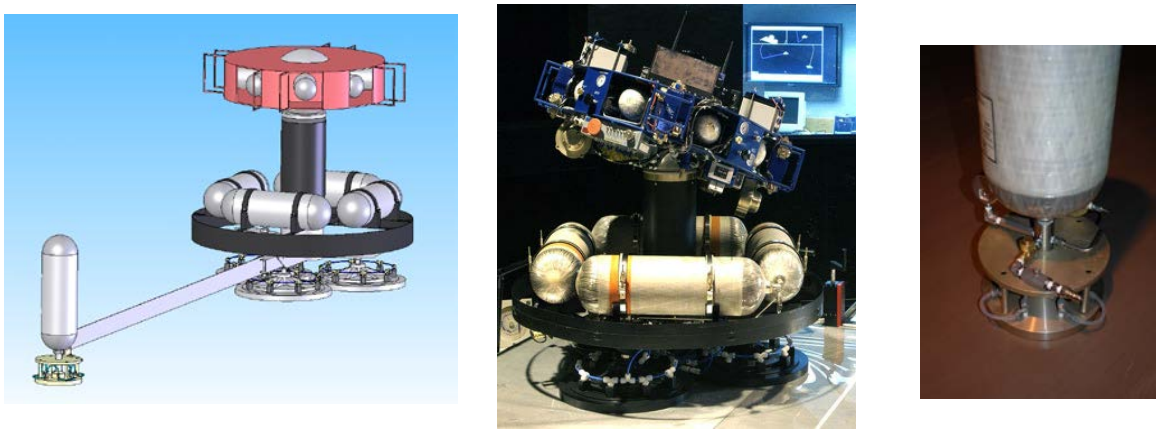

Figure 39. Sketch of components of test to be done in space simulator.

VIII. Conclusion

In conclusion, in this study we have investigated the structural dynamics and controllability aspects of an adaptive beam carrying an end-effector which, changing equilibrium phases is able to actively decouple the end-effector dynamics from the spacecraft dynamics during the surface contact phase. We have characterized the component level behavior via test and analysis and begun system level characterization. Component level characterization was achieved by analysis using two different phase transition constitutive models (Muller-Achenbach-Seelecke, and Dano-Hyer), and axial and bending tests of 1-D members involving thermal imaging and photo/videogrammetry. The experimental data was correlated with the results of the analytical model. System level multibody dynamic simulation includes a rigid spacecraft and end effector, and a flexible distributed boom which can be actuated during contact according to the phase-transition logic. System level experimental characterization includes a planar configuration of the system to eliminate gravity effects, with a robot SC and a hockey-puck on an air table, and an antagonistic pair of SMA wires to actuate the long beam during contact and to modulate the contact force in an adaptive manner. These experiments are currently being carried out in the Formation Control Testbed at JPL.

Acknowledgments

This research was carried out at the Jet Propulsion Laboratory, California Institute of Technology, under a contract with the National Aeronautics and Space Administration.

References

[1] Bayard, D. S. , Eisenman, D. : *Small Body Guidance, Navigation, and Control*, JPL Report D-36457, October 2006.

[2] Boyd, J.G., Lagoudas, D.C., *A Thermodynamical Constitutive Model for Shape Memory Materials. Part I. The Monolithic Shape Memory Alloy*, International Journal of Plasticity, Vol. 12, No. 6, pp. 805-842, 1996.

[3] COMSOL Multiphysics: User's Guide, Version 3.5a, COMSOL AB, November 2008.

[4] Dano, M.-L., Hyer, M. W., *SMA-Induced Snap-Through of Unsymmetric Fiber-Reinforced Composite Laminates*, International Journal of Solids and Structures, Vol. 40, pp. 5949-5972, 2003..

[5] Birman, V., *Review of Mechanics of Shape Memory Alloy Structures*, Applied Mechanics Reviews, Vol. 50, No. 11, Pt. 1, November 1997.

[6] Franzen, M.A., and Sears, M.A.: *The HERA Near-Earth Asteroid Sample Return Mission: an Overview*, Lunar and Planetary Science XXXIV (2003).

[7] Higuchi, K., Kawaguchi, J., Fujiwara, A., Okudaira, T., Yajima, S.: *Asteroid Sampling Mechanisms for MUSES-C*, NASA CP-2002/211505, Proceedings of the 36th Aerospace Mechanisms Symposium, Glenn Research Center, May 15-20, 2002.

[8] Massad, J.: *Macroscopic Models for Shape Memory Alloy Characterization and Design*, NCSU PhD Thesis, June 2003.

[9] Peffer, A., Fosness, E., Carpenter, B., and Denoyer, K., *On-Orbit Experiments and Applications of Shape Memory Alloy Mechanisms*, in Smart Structures and Materials 2000: Industrial and Commercial Applications of Smart Structures, Jack H. Jacobs, Editor, Proceedings of SPIE Vol. 3991 (2000).

[10] Seelecke, S., Muller, I.: *Shape Memory Alloy Actuators in Smart Structures: Modeling and Simulation*, Applied Mechanics Reviews, vol. 57. no.1, January 2004.

[11] Wayman, C.M., *Shape Memory and Related Phenomena*, Progress in Materials Science, Vol. 36, pp. 203-224, 1992.

[12] Jain, A., Balaram, J., Cameron, J., Guineau, J., Lim, C., Pomerantz, M., and Sohl, G. (2004). *Recent developments in the roams planetary rover simulation environment*. In Proceedings of 2004 IEEE Aerospace Conference, Big Sky, Montana.

[13] Jain, A., Cameron, J., Lim, C., and Guineau, J. (2006). *Simscape terrain modeling toolkit*. In Proceedings of Second Internatial Conference on Space Mission Challenges for Information Technology (SMC-IT 2006), Pasadena, USA.

[14] Hunt, K. and Crossley, F. (1975). Coefficient of restitution interpreted as damping in vibroimpact. Journal of Applied Mechanics, pages 440–445.

[15] Sohl, G. and Jain, A. (2005). *Wheel-terrain contact modeling in the roams planetary rover simulation*. In Proceedings of ASME International Design Engineering Technical Conference, Long Beach, USA.

[16] Quadrelli, M. B. , Backes, P., Wilkie, K., Giersch, L., Quijano, U., Mukherjee, R.: *Modeling and Testing of Phase Transition-Based Deployable Systems for Small Body Sample Capture*, presented at the 17th AIAA/ASME/AHS Adaptive Structures Conference, 4 - 7 May 2009, Palm Springs Convention Center, Wyndham Palm Springs. Palm Springs, California.

[17] Scharf, D.P., Hadaegh, F.Y., Keim, J.A., Morfopoulos, A.C., Ahmed, A., Brenman, Y., Vafaei, A., Shields, J.F., Bergh, C.F., and Lawson, P.R., *Flight-Like Ground Demonstrations of Precision Maneuvers for Spacecraft Formations*, AIAA Guidance, Navigation, & Control Conference, August, 2008.